Rest-frame UV spectroscopy of extreme [O III] emitters at $1.3 < z < 3.7$: toward a high-redshift UV reference sample for *JWST*

Mengtao Tang [1]*, Daniel P. Stark,[1] Jacopo Chevallard [2], Stéphane Charlot,[2] Ryan Endsley [1] and Enrico Congiu [3,4]

[1] *Steward Observatory, University of Arizona, 933 N Cherry Ave, Tucson, AZ 85721, USA*
[2] *Institut d'Astrophysique de Paris, Sorbonne Université, UPMC-CNRS, UMR7095, F-75014, Paris, France*
[3] *Departamento de Astronomía, Universidad de Chile, Camino del Observatorio 1515, Las Condes, Santiago, Chile*
[4] *Las Campanas Observatory – Carnegie Institution for Science, Colina el Pino, Casilla 601, La Serena, Chile*

ABSTRACT

Deep spectroscopy of galaxies in the reionization era has revealed intense C III] and C IV line emission (equivalent width, EW >15–20 Å). In order to interpret the nebular emission emerging at $z > 6$, we have begun targeting rest-frame ultraviolet (UV) emission lines in galaxies with large specific star formation rates (sSFRs) at $1.3 < z < 3.7$. We find that C III] reaches the EWs seen at $z > 6$ only in large sSFR galaxies with [O III]+Hβ EW >1500 Å. In contrast to previous studies, we find that many galaxies with intense [O III] have weak C III] emission (EW = 5–8 Å), suggesting that the radiation field associated with young stellar populations is not sufficient to power strong C III]. Photoionization models demonstrate that the spread in C III] among systems with large sSFRs ([O III]+Hβ EW >1500 Å) is driven by variations in metallicity, a result of the extreme sensitivity of C III] to electron temperature. We find that the strong C III] emission seen at $z > 6$ (EW >15 Å) requires metal-poor gas ($\simeq$ 0.1 $Z_{\odot}$), whereas the weaker C III] emission in our sample tends to be found at moderate metallicities ($\simeq 0.3 Z_{\odot}$). The luminosity distribution of the C III] emitters in our $z \simeq 1$–3 sample presents a consistent picture, with stronger emission generally linked to low-luminosity systems ($M_{\rm UV} > -19.5$) where low metallicities are more likely. We quantify the fraction of strong C III] and C IV emitters at $z \simeq 1$–3, providing a baseline for comparison against $z > 6$ samples. We suggest that the first UV line detections at $z > 6$ can be explained if a significant fraction of the early galaxy population is found at large sSFR (>200 Gyr^{-1}) and low metallicity (< 0.1 $Z_{\odot}$).

Key words: galaxies: evolution – galaxies: formation – cosmology: observations.

1 INTRODUCTION

Our understanding of galaxies in the reionization era has advanced considerably in the past decade following a series of multiwavelength imaging surveys conducted with the *Hubble Space Telescope* (*HST*, e.g. McLure et al. 2013; Bouwens et al. 2015; Finkelstein et al. 2015; Livermore, Finkelstein & Lotz 2017; Atek et al. 2018; Oesch et al. 2018). These campaigns have revealed thousands of galaxies thought to lie at $z > 6$, providing our first census of the star-forming sources thought responsible for reionization (see Stark 2016; Dayal & Ferrara 2018 for reviews). The *James Webb Space Telescope* (*JWST*) will soon build on this progress, delivering the first detailed spectroscopic investigation of $z > 6$ galaxies and opening the door for investigations of stellar populations and the build-up of metals in early star-forming systems.

The first glimpse of the nebular emission line properties of the $z > 6$ population has emerged in the last several years, providing a preview of the science that will be possible with *JWST*. Deep rest-frame ultraviolet (UV) spectra have revealed intense line emission from highly ionized species of carbon (C III], C IV; e.g. Stark et al. 2015a,

b, 2017; Laporte et al. 2017; Mainali et al. 2017; Hutchison et al. 2019), indicating a hard ionizing spectrum that is not seen in typical star-forming galaxies (SFGs) at lower redshifts. The origin of the hard photons remains a matter of debate, with some suggesting active galactic nuclei (AGNs) are required (Nakajima et al. 2018) and others suggesting that metal-poor massive star populations are sufficient (Stark et al. 2017). While direct constraints on the rest-frame optical spectra await *JWST*, progress has been made possible by *Spitzer*/The Infrared Array Camera (IRAC) broad-band photometry, with the [3.6] − [4.5] colours of $z > 6$ galaxies commonly revealing the presence of strong [O III]+Hβ nebular emission. The typical rest-frame equivalent widths (EWs) at $z \simeq 6 - 8$ (EW$_{\rm [O III] + H\beta} \simeq 600$–800 Å; e.g. Labbé et al. 2013; Smit et al. 2015; De Barros et al. 2019; Endsley et al. 2020) indicate both strong line emission and weak underlying continuum, a signpost of galaxies dominated by very young stellar populations (< 50 Myr), as expected for systems undergoing rapidly rising star formation histories.

Work is now underway to determine what these emission line properties are telling us about the reionization-era population. Central to these efforts are campaigns focused on galaxies with similar emission line properties at lower redshifts where they can be studied in greater detail. Sizeable samples of $z \simeq 1$–2 galaxies with large

* E-mail: tangmtasua@email.arizona.edu

[O III]+Hβ EWs have been identified in broadband imaging and grism spectroscopy (e.g. Atek et al. 2011; van der Wel et al. 2011; Maseda et al. 2013, 2014), revealing a young population of low-mass galaxies with high densities of massive stars. In Tang et al. (2019, hereafter T19), we built on these studies, targeting the strong rest-frame optical lines in 227 galaxies with [O III]+Hβ EW = 300–3000 Å. The spectra revealed that the ionizing efficiency of galaxies (defined as the ratio of the hydrogen ionizing photon production rate and the far-UV continuum luminosity at 1500 Å) increases with the [O III] EW. The ionization state of the nebular gas (as probed by the [O III]/[O II] flux ratio, hereafter O32) was also found to increase with the [O III] EW, suggesting very large ionization parameters in the most extreme line emitters. Investigations of nearby galaxies show nearly identical trends (Chevallard et al. 2018), suggesting little redshift evolution in the trends with [O III] EW. Taken together, these studies indicate that very hard spectra and highly ionized gas conditions are common in a short window following a burst of star formation in low-mass galaxies.

Progress has also been made in our understanding of the rest-frame UV nebular line detections. A series of *HST*/UV spectroscopy programs have investigated the stellar populations and gas conditions required to power C III] and C IV in nearby SFGs (Senchyna et al. 2017, 2019; Berg et al. 2019). The results have revealed that C III] is intense in galaxies with moderately low metallicities ($< 0.4\,Z_\odot$) and large specific star formation rates (sSFRs), with the C III] EW increasing in lockstep with the [O III] EW (e.g. Rigby et al. 2015; Senchyna et al. 2017, 2019). Both nebular C IV and He II appear in lower metallicity galaxies ($< 0.1\,Z_\odot$), provided the sSFR (or Hβ EW) is large enough to guarantee a significant population of high-mass stars (Senchyna et al. 2019). The local C III] and C IV trends have been successfully explained in the context of photoionization models (Jaskot & Ravindranath 2016; Gutkin, Charlot & Bruzual 2016; Byler et al. 2018; Plat et al. 2019). But in spite of these successes, the local studies have struggled to identify galaxies with C III] and C IV EWs as large as seen at $z > 6$, making it challenging to interpret the emerging body of reionization-era spectra.

Rest-frame UV surveys at $z \simeq 1–4$ have provided a viable way forward, leading to the discovery of a significant number of intense UV line emitters in the last decade (Erb et al. 2010; Stark et al. 2014; De Barros et al. 2016; Amorín et al. 2017; Maseda et al. 2017; Vanzella et al. 2017; Berg et al. 2018; Le Fèvre et al. 2019; Feltre et al. 2020). To date, nearly all $z \simeq 1–4$ galaxies with UV line properties similar to those seen at $z > 6$ (i.e. EW$_{\mathrm{C\,III]}} > 20$ Å or EW$_{\mathrm{C\,IV}} > 20$ Å) appear to be AGN (Nakajima et al. 2018; Le Fèvre et al. 2019), leading to the suggestion that stellar radiation fields may be incapable of powering the line emission seen in the reionization era. Motivated by the relationship between C III] and [O III] EW (Maseda et al. 2017; Du et al. 2020), efforts targeting SFGs have begun to focus on very young (< 10 Myr) stellar populations with the most extreme optical line emission (EW$_{\mathrm{[O\,III]}+\mathrm{H}\beta} > 1500$ Å), with one recently discovered system identified in this manner displaying UV line properties that are nearly identical to those discovered in the reionization era (i.e. EW$_{\mathrm{C\,III]}} > 20$ Å; Mainali et al. 2020). This finding suggests that stellar populations may be sufficient to power the nebular emission seen at $z > 6$, but without larger samples, it is impossible to generalize to the broader population of young galaxies with EW$_{\mathrm{[O\,III]}+\mathrm{H}\beta} > 1500$ Å.

Motivated by this shortcoming, work is now underway to build large rest-frame UV spectral data bases of galaxies with extreme optical line emission. The first statistical measures of the rest-frame UV spectral properties of galaxies selected to have large EW [O III]+Hβ emission have emerged recently (Maseda et al. 2017; Du et al. 2020). Here, we describe results of an ongoing spectroscopic campaign aimed at building on this progress. In particular, we discuss rest-frame UV spectra of 138 extreme [O III] emitting galaxies at 1.3 $< z <$ 3.7 together with a smaller sample of 4 $< z <$ 6 galaxies. Our survey includes 26 galaxies with the most extreme [O III]+Hβ EWs (> 1500 Å), nearly 9 times greater than that in previous studies. Our goals are twofold. First we aim to build a large enough sample of $z \simeq 1–3$ galaxies with [O III]+Hβ EW = 1000–2000 Å such that we can assess whether the C III] intensities seen at $z > 6$ (i.e. C III] EW >20 Å) commonly arise in galaxies with extremely young stellar populations, as suggested by the single galaxy identified in Mainali et al. (2020). And secondly, we seek to quantify the rate at which very metal-poor stellar populations ($< 0.1\,Z_\odot$) appear among low-mass extreme line emitting galaxies at $z \simeq 1–3$ via measurement of the fraction of nebular C IV emitters (with line ratios indicating a stellar origin) in our spectroscopic sample. This will provide a baseline for comparison against future measurements at $z > 6$, giving the control needed to track the rise of low-metallicity massive-star populations in early galaxies matched to our sample in M_{UV} and sSFR.

The organization of this paper is as follows. We describe the spectroscopic sample and rest-frame UV spectroscopic observations, as well as our photoionization modelling procedures in Section 2. We then present the rest-frame UV spectra of our $1.3 < z < 6$ galaxies in Sections 3, and the physical properties inferred from spectra in Section 4. We discuss the implications of these results in Section 5 and summarize our conclusions in Section 6. We adopt a Λ-dominated, flat universe with $\Omega_\Lambda = 0.7$, $\Omega_{\mathrm{M}} = 0.3$, and $H_0 = 70$ km s^{-1} Mpc^{-1}. All magnitudes in this paper are quoted in the AB system (Oke & Gunn 1983), and all EWs are quoted in the rest frame.

2 OBSERVATIONS AND ANALYSIS

In this work, we aim to investigate the rest-frame UV spectra of galaxies with extreme EW optical line emission (extreme emission line galaxies, EELGs). We primarily focus on the extreme [O III] line emitting galaxies at $z = 1.3–3.7$, obtaining rest-frame UV spectra via ground-based optical spectrographs. In addition, we present near-infrared spectroscopy of a subset of sources at $z \sim 4–6$. The spectroscopic observations of each sample are described in Sections 2.1 and 2.2, respectively. We then describe the photoionization modelling we apply to our sample in Section 2.3.

2.1 Optical spectroscopy of z = 1.3–3.7 EELGs

The rest-frame UV spectra presented in this subsection build on a large spectroscopic effort to obtain rest-frame optical spectra of extreme [O III] emitters at $z = 1.3–3.7$ in the Cosmic Assembly Near-infrared Deep Extragalactic Legacy Survey (CANDELS) fields (T19; Tang et al., in preparation) and the recent rest-frame UV spectroscopic surveys presented in Du et al. (2020) and Mainali et al. (2020). We direct the reader to T19 for the full description of the sample selection and the follow-up near-infrared (rest-frame optical) spectroscopic observations. The extreme [O III] emitters are required to have large rest-frame [O III] $\lambda\lambda$4959, 5007 EWs with values $\simeq$ 300–2000 Å, which are chosen to match the range expected to be common in reionization-era galaxies (e.g. Endsley et al. 2020). In order to measure the rest-frame UV emission lines of extreme [O III] emitters at $z = 1.3–3.7$, we have been conducting optical spectroscopic observations. Data were taken over three observing runs between 2018 and 2019 with optical spectrographs on the Magellan telescopes and the Multiple Mirror Telescope (MMT).

Table 1. Summary of optical spectroscopic observations of extreme [O III] emitters at $z = 1.3$–3.7. Column (1): CANDELS field; column (2): number of science targets on each mask, alignment stars, and slit stars are not included; column (3): right ascension of the mask centre; column (4): declination of the mask centre; column (5): position angle of the mask; column (6): instrument being used; column (7): total exposure time of each observing run; and column (8): average seeing during the observation, in FWHM.

Field	Number of targets	RA (hh:mm:ss)	Dec. (dd:mm:ss)	PA (deg)	Instrument	Exposure time (h)	Average seeing (arcsec)
(1)	(2)	(3)	(4)	(5)	(6)	(7)	(8)
COSMOS	60	10:00:21	02:18:00	-80	Magellan/IMACS	5.7	0.8
UDS	54	02:17:26	$-05:12:13$	-8	Magellan/IMACS	3.0	0.8
UDS	24	02:17:26	$-05:05:40$	-86	MMT/Binospec	5.0	1.2

The majority of our optical spectroscopic follow-up program is conducted using the Inamori-Magellan Areal Camera & Spectrograph (IMACS; Dressler et al. 2011) on the Magellan Baade telescope. We use IMACS in multislit spectroscopy mode. We designed two masks in the Cosmic Evolution Survey (COSMOS) field and the Ultra Deep Survey (UDS) field utilizing the 'MASKGEN' software, targeting 114 extreme [O III] emitters (EW$_{[O III]\lambda\lambda 4959, 5007}$ > 300 Å) at $z \simeq 1.3$–3.7. The targets were placed on the IMACS masks using a similar selection function introduced in section 2.2 of T19. We adjust the target priority based on the [O III] EWs inferred from *HST* grism spectra (at $z = 1.3$–2.4; T19) or the *K*-band flux excess (at $z = 3.1$–3.7; Tang et al. in preparation). Objects with the largest EWs ([O III] EW >1000 Å) are very rare, and thus we give the highest priority to the largest EW [O III] line emitting galaxies. In addition, we are particularly interested in comparing the properties derived from rest-frame UV spectroscopy and those from rest-frame optical spectroscopy. Therefore, we increase the priority of objects whose rest-frame optical spectra have been taken from our near-infrared spectroscopic follow-up program (T19; Tang et al., in preparation).

The details of the IMACS observations are summarized in Table 1. We used the 300 lines mm^{-1} grism blazed at 17.5° on the *f/2* camera. The grism provides wavelength coverage from 3900 to 10 000 Å, covering UV metal lines including C IV, O III], and C III], as well as Lyα emission line at $z > 2.2$ and [O II] $\lambda\lambda 3727$, 3729 emission lines at $z < 1.68$. The slit length and width of our IMACS mask were set to 6.0 and 1.0 arcsec, respectively. The 1.0 arcsec slit width results in a spectral resolution of 6.7 Å for the entire wavelength coverage. For the mask targeting the COSMOS field, we placed 60 extreme [O III] emitters at $z \simeq 1.3$–3.7 with [O III] $\lambda\lambda 4959$, 5007 EW $\simeq$ 300–2000 Å. The targets have i_{814}-band magnitude from 23.1 to 26.7, with a median value of 25.2. We observed this mask on 2019 March 06 and 07 for a total on-source integration time of 5.7 hours with an average seeing of 0.8 arcsec. We placed 54 extreme [O III] emitters at $z \simeq$ 1.3–3.7 with [O III] $\lambda\lambda 4959$, 5007 EW $\simeq$ 300–1600 Å on the mask targeting the UDS field. The i_{814}-band magnitudes of these targets have a range from 23.8 to 26.9 (median $i_{814} = 25.5$). This mask was observed on 2019 October 30 for an integration time of 3 hours with seeing of 0.8 arcsec. Each mask contains two slits stars to compute the absolute flux calibration. We also observed spectrophotometric standard stars at a similar airmass in each observing run in order to correct the instrumental response.

We reduced the IMACS spectra using the publicly available data reduction pipeline Carnegie Observatories System for MultiObject Spectroscopy[1] (Dressler et al. 2011; Oemler et al. 2017). During the observing runs, flat fields were obtained using quartz high

lamps, and arcs were obtained using HeNeAr lamps. The pipeline performs bias subtraction, flat-fielding, wavelength calibration, sky subtraction, and extracts the 2D spectra. We created 1D spectra from the reduced 2D spectra using a boxcar extraction, with the extraction aperture matched to the spatial profile of the object. We derived the transmission curve from the observed standard star spectra and corrected the instrumental response. Slit loss corrections were performed following the similar procedures in T19 (see also Kriek et al. 2015). We derived the spatial profile of each target from its *HST* F606W postage stamp, and computed the fraction of the light within the slit to that of the total spatial profile. The flux of each spectrum was then divided by the in-slit light fraction measured for each object. Finally, the absolute flux calibration was performed using the slit stars, by comparing the slit-loss corrected count rates of slit star spectra with the flux in the Skelton et al. (2014) catalogues. For objects on the mask targeting the COSMOS field, the median 3σ line flux sensitivity of the IMACS spectra is 3.6×10^{-18} erg s^{-1} cm^{-2} (assuming a line width of 13.4 Å, i.e. 2 times the spectral resolution) in the wavelength range (4800–6300 Å) where C III] (at $z \sim 2$) or Lyα (at $z \sim 3$) is situated. This flux limit enables us to detect emission lines (3σ) with rest-frame EW $\sim$1, 4, and 17 Å for the sources with the brightest (23.1), median (25.2), and the faintest (26.7) continuum magnitudes. For objects on the mask targeting the UDS field, we reached a median 3σ line flux sensitivity of 6.9×10^{-18} erg s^{-1} cm^{-2} in 4800–6300 Å. This sensitivity provides 3σ line EW limits of $\sim$2, 11, and 41 Å for the sources with the brightest (23.8), median (25.5), and the faintest (26.9) continuum magnitudes.

We also obtained optical spectra from the Binospec (Fabricant et al. 2019) on the MMT with multislit spectroscopy mode. We designed one mask in the UDS field using the 'BinoMask' software. Twenty-four extreme [O III] emitters ([O III] $\lambda\lambda 4959$, 5007 EW $\simeq$ 700–2500 Å) were placed on the mask with the same selection function used in Magellan/IMACS observations. The targets have i_{814} magnitude from 23.7 to 26.7 (median $i_{814} = 25.7$). Spectra were taken using the 270 lines mm^{-1} grism blazed at 5.5°, with wavelength coverage from 3850 to 9000 Å. The slit width was set to 1.0 arcsec, which results in a spectral resolution of $R = 1340$. We observed this mask on 2018 October 18 and November 03 for a total integration time of 5 hours with an average seeing of 1.2 arcsec. The mask contains two slit stars to derive absolute flux calibration, and standard stars were observed to correct the instrumental response. We summarize the details of the Binospec observations in Table 1.

We reduced the Binospec spectra using the publicly available data reduction pipeline[2] (Kansky et al. 2019). The pipeline performs flat-fielding, wavelength calibration, and sky subtraction.

---

[1] https://code.obs.carnegiescience.edu/cosmos The acronyms of the IMACS data reduction pipeline Carnegie Observatories System for MultiObject Spectroscopy, COSMOS, is incidentally the same as that of the Cosmic

Evolution Survey. When mentioning COSMOS throughout the paper, we only refer to the Cosmic Evolution Survey.
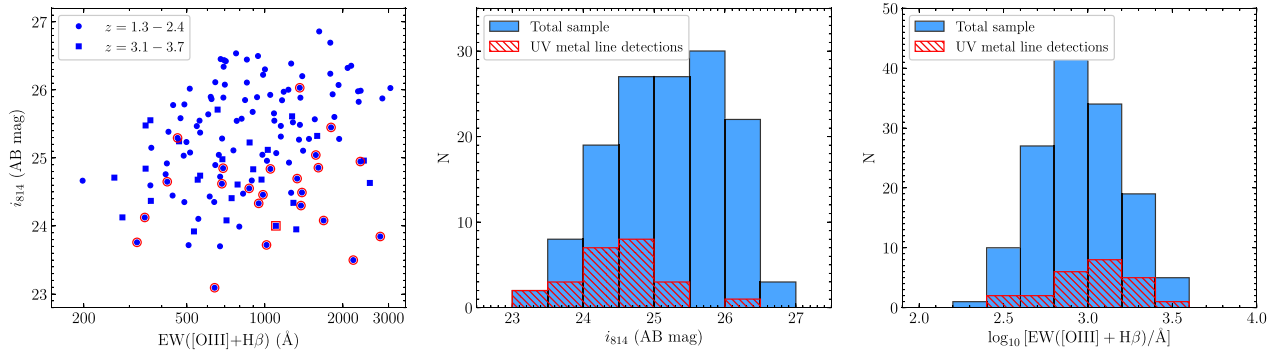
[2] https://bitbucket.org/chil_sai/binospec

Figure 1. *HST* F814W magnitude and [O III]+Hβ EW distribution of the 138 extreme [O III] emitters at $z = 1.3$–3.7 in our spectroscopic sample. Left-hand panel: F814W magnitudes and [O III]+Hβ EWs of the 138 galaxies (objects at $z = 1.3$–2.4 are shown by blue circles, and objects at $z = 3.1$–3.7 are shown by blue squares). Those sources with UV metal line detections are additionally demarcated by larger red circles or squares. Middle panel: F814W magnitude distributions of the total extreme [O III] emitter sample (solid blue) and the subset with UV metal emission line detections presented in Section 3.1 (dashed red). Right-hand panel: [O III]+Hβ EW distributions of the total sample (solid blue) and the subset with UV metal line detections (dashed red).

Before extracting the 2D spectra, the pipeline corrects atmospheric extinction and instrumental response using the sensitivity curve derived from observations of standard stars. We extracted the 1D spectra using a boxcar extraction. The absolute flux calibration was performed using slit stars, and slit-loss correction was performed following the same procedures used in Magellan/IMACS observations. The median 3σ line flux sensitivity of our Binospec spectra is 7.2×10^{-18} erg s^{-1} cm^{-2} in 4800–6300 Å, providing 3σ line EW limits of ∼2, 14, and 34 Å for the sources with the brightest (23.7), median (25.7), and the faintest (26.7) continuum magnitudes.

Our observations described above obtained optical (rest-frame UV) spectra for 138 extreme [O III] emitters at $z = 1.3$–3.7. The i_{814} magnitude distribution of these 138 galaxies are shown in Fig. 1. We also add available near-infrared (rest-frame optical) spectra which provide useful constraints on the ionizing radiation fields and the interstellar medium (ISM) conditions. We have obtained ground-based near-infrared spectra for 33 of the 138 sources (T19; Tang et al., in preparation), with strong [O III] λ5007 or Hα emission lines detected at signal-to-noise ratio (S/N) >5. Among these 33 objects, 24 have the full suite of strong rest-frame optical emission line detections ([O II], Hβ, [O III], Hα), allowing us to measure ionization and metallicity sensitive line ratios (i.e. [O III]/[O II]). For the remaining objects without ground-based near-infrared spectroscopic observations, we utilize the Hβ, [O III], or Hα emission lines measured from *HST* grism near-infrared spectra (Momcheva et al. 2016) if the grism S/N is larger than 5. This results in a sample of 116 (of 138) galaxies with [O III] flux measurements. We then compute [O III] EWs following T19 and (Tang et al., in preparation). In Section 5, we will discuss the correlations between rest-frame UV spectral properties and rest-frame optical properties (i.e. [O III] λ5007 EW).

2.2 Near-infrared spectroscopy of z ∼ 4–6 EELGs

We have additionally obtained rest-frame UV spectra for a smaller number of extreme optical line emitter candidates at $z \sim 4$–6. For galaxies in this redshift range, strong rest-frame optical emission lines (Hα, [O III]) are situated in *Spitzer*/IRAC 3.6 or 4.5 μm band, allowing us to identify extreme optical line emitters via large flux excesses in the [3.6] or [4.5] filters. Recent studies (e.g. Shim et al. 2011; Stark et al. 2013; Rasappu et al. 2016) reveal that extreme Hα emitters at $3.8 < z < 5.0$ ($5.1 < z < 5.4$) show blue (red) [3.6] − [4.5] colours, since the Hα emission line is within the

[3.6] ([4.5]) filter while the [4.5] ([3.6]) filter is dominated by rest-frame optical continuum. For galaxies at $5.4 < z < 6.0$, [O III]+Hβ and Hα+[N II] emission lines are situated in [3.6] and [4.5] filters, respectively. In this subsection, we first describe selection of a sample of extreme optical line emitter candidates at $z \sim 4$–6 using IRAC colour excess methods, then describe the near-infrared (rest-frame UV) spectroscopic observations of a subset of the sources in this sample.

Our $z \sim 4$–6 targets were selected from public samples of Lyman break galaxies (LBGs) with spectroscopic or photometric redshift measurements. Taking advantage of the spectroscopic redshifts provided in Stark et al. (2013) and Rasappu et al. (2016), we identified a subset of sources at $3.8 < z_{\rm spec} < 5.0$ and $5.1 < z_{\rm spec} < 5.4$. Redshifts in the above papers are derived from Lyα emission lines or UV absorption lines. We also selected LBGs with photometric redshifts at $3.8 < z < 6.0$ (and with 1σ photo-z uncertainty $\delta z < 0.1$ to ensure robust redshift estimates) from Bouwens et al. (2015), where the redshifts are computed using EAZY (Brammer, van Dokkum & Coppi 2008). To ensure self-consistent astrometry, we matched the coordinates of all the sources with spectroscopic or photometric redshifts to Skelton et al. (2014) catalogues. To efficiently identify EELGs, we required [3.6] − [4.5] < −0.3 for sources at $3.8 < z < 5.0$ and [3.6] − [4.5] > 0.3 for sources at $5.1 < z < 5.4$. We also required S/N >5 for the [3.6] and [4.5] fluxes so that the Hα EWs can be accurately derived from IRAC colours. The above [3.6] − [4.5] colour cuts correspond to Hα+[N II]+[S II] EW >500 Å, which is greater than the average Hα EW estimated for SFGs in the reionization era (Labbé et al. 2013). For sources at $5.4 < z < 6.0$, we do not apply an IRAC colour cut since strong rest-frame optical emission lines are within both [3.6] and [4.5] filters.

We use the catalogue of $z \sim 4$–6 extreme optical line emitter candidates described above as input for our near-infrared spectroscopic observations. The spectra presented in this paper were obtained using the Multi-object Spectrometer for Infrared Exploration (MOSFIRE; McLean et al. 2012) on the Keck I telescope. We observed two masks on 2015 November 30, targeting six sources in the GOODS-S field and five sources in the COSMOS field. The remainder of the mask was filled with sources discussed in previous publications (Stark et al. 2017, T19). The slit widths were set to 0.7 arcsec, resulting in a spectral resolution of $R = 3388$ ($\Delta\lambda \simeq 2.9$ Å at the blue end, ∼9716 Å, and $\Delta\lambda \simeq 3.3$ Å at the red end, ∼11 250 Å).

For the mask targeting the GOODS-S field, we observed six objects at $3.8 < z < 5.0$. The primary targets of this mask are two

Table 2. Summary of near-infrared spectroscopic observations of extreme optical line emitters at $z \sim 4$–6. Column (1): Target ID; column (2): spectroscopic redshift derived from Lyα emission line; column (3): photometric redshift from Skelton et al. (2014); column (4): right ascension of the mask centre; column (5): declination of the mask centre; column (6): J-band (*HST* F125W) magnitude; column (7): [3.6] − [4.5] colours for galaxies at $3.8 < z < 5.0$, which are used to estimate Hα EW; column (8): on-source integration time; and column (9): average seeing during the observation, in FWHM.

Target	$z_{Ly\alpha}$	z_{phot}	RA (hh:mm:ss)	Dec. (dd:mm:ss)	J_{125} (mag)	[3.6] − [4.5] (mag)	Exposure time (h)	Average seeing (arcsec)
(1)	(2)	(3)	(4)	(5)	(6)	(7)	(8)	(9)
COSMOS-18502	...	4.58	10:00:16.82	02:22:03.4	24.6	−0.30	2.4	0.74
COSMOS-19732	...	4.70	10:00:17.80	02:22:46.8	24.1	−0.72	2.4	0.74
COSMOS-11116	...	5.62	10:00:24.48	02:17:33.1	25.7	...	2.4	0.74
COSMOS-15365	...	5.64	10:00:22.88	02:20:10.8	24.9	...	2.4	0.74
COSMOS-20187	...	5.73	10:00:16.56	02:23:02.6	26.2	...	2.4	0.74
GOODS-S-36712	...	4.74	03:32:10.32	− 27:44:25.4	25.3	−0.28	3.2	0.94
GOODS-S-38450	...	4.58	03:32:09.06	− 27:43:51.8	25.2	−0.20	3.2	0.94
GOODS-S-39157	...	4.17	03:32:09.32	− 27:43:38.8	25.4	−0.08	3.2	0.94
GOODS-S-40887	...	4.50	03:32:13.24	− 27:43:08.4	25.7	−0.17	3.2	0.94
GOODS-S-41253	...	4.28	03:32:11.30	− 27:43:01.3	26.0	−0.45	3.2	0.94
GOODS-S-46692	4.811	4.66	03:32:10.03	− 27:41:32.6	24.9	−0.33	3.2	0.94

extreme Hα emitting candidates, GOODS-S-46692 and GOODS-S-41253. GOODS-S-46692 is a bright galaxy ($J_{125} = 24.9$) with a spectroscopic redshift derived from Lyα emission, $z_{Ly\alpha} = 4.811$ (Vanzella et al. 2008), and IRAC colour [3.6] − [4.5] = −0.33. GOODS-S-41253 is fainter ($J_{125} = 26.0$) with photometric redshift of $z_{phot} = 4.28$ and IRAC colour [3.6] − [4.5] = −0.45. We also added four sources ($J_{125} = 25.2$–25.7) with photometric redshifts in the range $z_{phot} = 4.1$–4.8 and less extreme IRAC colours ([3.6] − [4.5] = −0.1 to −0.3) as fillers of this mask. We observed in Y band, for a total on-source integration time of 3.2 hours with an average seeing of 0.94 arcsec. The spectral wavelength coverage is from $\sim$9716 to $\sim$11 250 Å, allowing constraints on C III] $\lambda\lambda$1907, 1909 for the chosen targets.

For the mask targeting the COSMOS field, we observed five objects with photometric redshifts at $3.8 < z_{phot} < 6.0$. Two bright targets ($J_{125} = 24.1$–24.6) have photometric redshifts in the range $z = 4.5$–4.7 with blue IRAC colours [3.6] − [4.5] = −0.30 to −0.72. The other three targets ($J_{125} = 24.9$–26.2) have photometric redshifts ($z = 5.6$–5.8) where both IRAC filters are contaminated by emission lines. We observed the COSMOS mask in Y band for a total on-source integration time of 2.4 hours with an average seeing of 0.74 arcsec. The observations enable constraints on the C III] $\lambda\lambda$1907, 1909 line strengths for targets at $z = 4.5$–4.7 and O III] $\lambda\lambda$1661, 1666 for those at $z = 5.6$–5.8. Both of the masks were filled with $z \simeq 2$ extreme [O III] line emitting galaxies, which have been discussed in T19. We also placed two slit stars on each mask for absolute flux calibration, and we obtained the telluric star spectrum in order to correct the atmosphere absorption and instrument response. For both masks, we performed a dither pattern of ± 1.5 arcsec along the slit for sky subtraction. The near-infrared spectroscopic observations of $z \sim 4$–6 extreme optical line emitter candidates are summarized in Table 2.

The spectra were reduced using the publicly available MOS-FIRE Data Reduction Pipeline (DRP[3]). The DRP performs flat-fielding, wavelength calibration, and background subtraction before extracting 2D spectra. We corrected the atmosphere absorption and instrument response using the spectrum of a telluric star, and performed slit-loss correction the same way as described in T19 (see also Kriek et al. 2015). The absolute flux calibration was performed using the spectra counts and photometric flux of slit stars.

We extracted 1D spectra using boxcar extraction with an aperture matched to the spatial profile of the object. Assuming a line width of 6–7 Å (2 times the spectral resolution), the median 5σ line flux sensitivity is 2.6 (3.2) $\times 10^{-18}$ erg s^{-1} cm^{-2} for spectra on the mask targeting the GOODS-S (COSMOS) field. We will present the results of our near-infrared spectroscopy of $z \sim 4$–6 targets in Section 3.2.

2.3 Photoionization modelling

We utilize photoionization models to investigate the physical properties of the EELGs in our rest-frame UV spectroscopic sample. We fit the broad-band photometry and observed emission lines from our objects using the Bayesian spectral energy distribution (SED) modeling and interpreting tool BEAGLE (version 0.23.0; Chevallard & Charlot 2016). The broad-band photometry is obtained from the 3D-HST catalogues (Skelton et al. 2014), and we use the multiwavelength data covering 0.3–2.5 μm. For each galaxy, we remove fluxes in filters that lie blueward of Lyα to avoid introducing uncertain contributions from Lyα emission and Lyα forest absorption. We simultaneously fit the available rest-frame UV (C IV, O III], C III]; see Section 3) and optical ([O II], Hβ, [O III], Hα) emission line fluxes. BEAGLE adopts the photoionization models of SFGs presented in Gutkin et al. (2016), which combines the latest version of Bruzual & Charlot (2003) stellar population synthesis (SPS) models with the photoionization code CLOUDY (Ferland et al. 2013) to describe the emission from stars and interstellar gas. The SPS models, which are described in more detail in Vidal-García et al. (2017, see their section 2.1), incorporate updated stellar-evolution calculation by Bressan et al. (2012) for stars with initial masses up to 350 M$_\odot$ (Chen et al. 2015), combined with libraries of stellar spectra from various sources. In fitting the data, we will explore whether the models powered by stars can reproduce the emission line fluxes and SEDs of the sources in our spectroscopic sample. The fits will constrain the stellar population parameters (e.g. stellar mass, age, and sSFR) as well as the ionized gas properties (e.g. metallicity and ionization parameter).

We assume a constant star formation history, parametrizing the maximum stellar age in the range from 1 Myr to the age of the universe at the given redshift. For galaxies with spectroscopic redshifts measured from rest-frame UV or optical spectra, we fix the redshift of each object to its spectroscopic redshift. For sources with photometric redshift measurements only, we allow the model galaxy
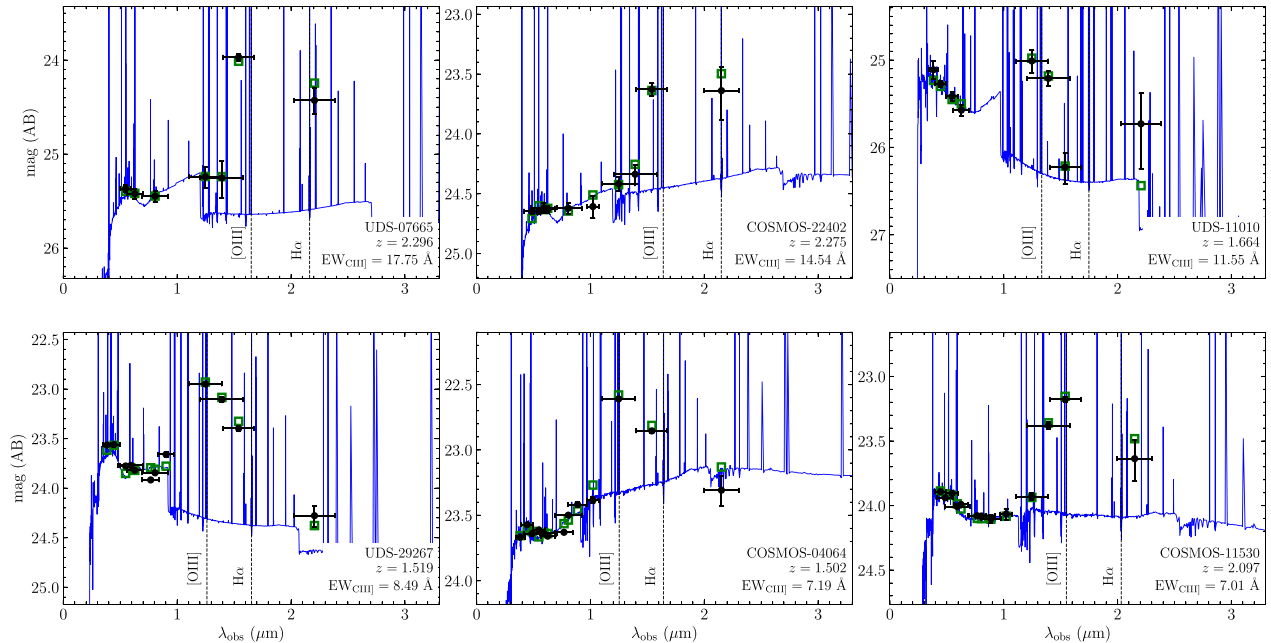
[3] https://keck-datareductionpipelines.github.io/MosfireDRP

Figure 2. Examples of the broadband SEDs of $z = 1.3$–3.7 extreme [O III] emitters with rest-frame UV metal line detections. Observed broadband photometry is shown as solid black circles. The best-fitting SED models inferred from BEAGLE are plotted by solid blue lines, and synthetic photometry is presented by open green squares.

redshift to vary in the 1σ confidence interval of photo-z for each object. We adopt a Chabrier (2003) initial mass function and allow the metallicity to vary in the range $-2.2 \leq \log(Z/Z_\odot) \leq 0.25$ ($Z_\odot = 0.01524$; Caffau et al. 2011). The interstellar metallicity is assumed to be the same as the stellar metallicity ($Z_{ISM} = Z_\star$) for each galaxy. We consider models with an electron density of $n_e = 100$ cm^{-3}, which is consistent with the average density inferred from typical SFGs at $z \sim 2$ (e.g. Sanders et al. 2016; Steidel et al. 2016). We adjust the ionization parameter U and the dust-to-metal mass ratio ξ_d in the range $-4.0 \leq \log U \leq -1.0$ and $0.1 \leq \xi_d \leq 0.5$, respectively. We also consider models with a set of carbon-to-oxygen abundance ratios (C/O =0.10, 0.27, 0.52, 0.72, and 1.00 (C/O)$_\odot$, where the solar value (C/O)$_\odot$ = 0.44). To account for the effect of dust attenuation in the neutral ISM, we assume the Calzetti et al. (2000) extinction curve. We adopt an exponential distribution prior on the V-band dust attenuation optical depths, fixing the fraction of attenuation optical depth arising from dust in the diffuse ISM to $\mu = 0.4$ (Chevallard & Charlot 2016). Finally, we adopt the prescription of Inoue et al. (2014) to include the absorption of IGM.

With the above parametrization, we fit the SEDs and available emission line constraints for the $z \sim 1$–6 EELGs in our sample using the BEAGLE tool. For each free parameter described above, we adopt the median of the posterior probability distribution as the best-fitting value. In Fig. 2, we overplot the best-fitting BEAGLE models on the observed broad-band SEDs. The models are able to reproduce the observed SEDs and nebular emission line fluxes. We show the best-fitting stellar population properties (stellar mass, sSFR, and stellar age) of the 138 extreme [O III] emitters at $z = 1.3$–3.7 in Fig. 3, highlighting the distribution for the subset of sources with UV line detections. Similar to what has been demonstrated in T19, galaxies with largest [O III] EWs have the lowest stellar masses, the largest sSFRs, and the youngest stellar ages. Objects with EW$_{[O III] + H\beta} = 1500$–3000 Å show much larger sSFRs (median value of 218 Gyr^{-1}) and younger luminosity-weighted stellar ages (median of 5 Myr, assuming a constant star formation history) than

those with EW$_{[O III] + H\beta} = 600$–800 Å (median sSFR =26 Gyr^{-1} and median age =37 Myr). The latter subset corresponds to the average EW of $z \sim 7$–8 galaxies (Labbé et al. 2013; De Barros et al. 2019; Endsley et al. 2020), whereas the more extreme optical line emitters are present in significant numbers at $z > 6$ (Smit et al. 2014, 2015; Endsley et al. 2020), often associated with strong rest-frame UV line emission (Stark et al. 2017; Hutchison et al. 2019). Here, we note that the young ages only refer to the stellar populations that are dominating the rest-frame UV and optical SED and do not exclude the presence of an underlying older stellar population.

The underlying rest-frame UV continuum predicted by BEAGLE is used to compute the UV emission line EWs for the objects without reliable continuum measurement from spectra as described in Section 3. For galaxies at $z \sim 4$–6 in our spectroscopic sample, BEAGLE can successfully reproduce the large IRAC flux excess caused by nebular emission. We infer the Hα and [O III] $\lambda5007$ EWs for our $z \sim 4$–6 sources from BEAGLE models since their rest-frame optical spectra are not visible with current facilities. We will discuss the constraints inferred from photoionization modelling in Section 4.

3 RESULTS

Here, we describe nebular emission line constraints made possible by the rest-frame UV spectra we have obtained for our EELGs at $z = 1.3$–3.7 (Section 3.1) and those we have observed at $z \sim 4$–6 (Section 3.2).

3.1 Rest-frame UV spectra at z = 1.3–3.7

We characterize the rest-frame UV emission line strengths for the 138 extreme [O III] emitters in our $z = 1.3$–3.7 sample described in Section 2.1. The redshifts of the majority (116) of these 138 sources were computed by fitting the [O III] $\lambda5007$ emission line from the ground-based (T19) or *HST* grism-based (Momcheva et al. 2016)
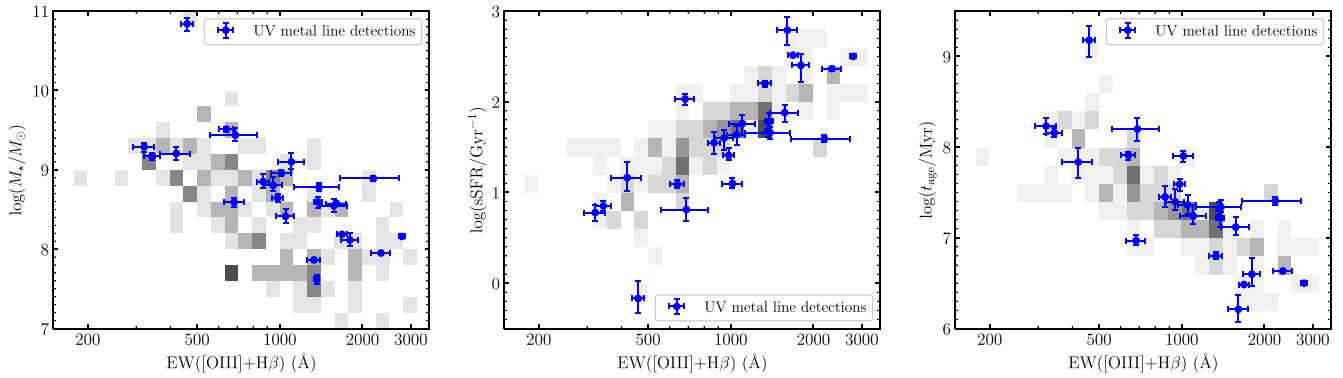
Figure 3. Stellar mass (left panel), sSFR (middle), and stellar age (right) as a function of [O III]+Hβ EW for the 138 extreme [O III] emitters at $z = 1.3$–3.7 in our spectroscopic sample. The properties are derived from photoionization modelling using BEAGLE. The shaded regions represents the number of galaxies in bins of [O III]+Hβ EW and stellar mass, sSFR, or age, with a darker colour indicates a larger number. We overplot the 24 galaxies with rest-frame UV line detections in our sample (see Section 3.1) with blue circles.

near-infrared spectra. For a subset (22) of objects at $z = 3.1$–3.7 identified by K_s-band excess (see Section 2.1), we do not yet have a rest-frame optical spectroscopic redshift. For these sources, we use the Lyα line to compute the redshift if it is available, and otherwise we rely on the photometric redshift measurements from the Skelton et al. (2014) catalogues. Using the measured redshifts, we search for rest-frame UV emission lines including the blended C IV λ1549 doublet, He II λ1640, O III] $\lambda\lambda$1661, 1666, Si III] $\lambda\lambda$1883, 1892, the blended C III] λ1908 doublet, and Mg II $\lambda\lambda$2796, 2803.

Emission line fluxes are determined from the extracted 1D spectra. If an emission line feature is well-detected (S/N >5), we apply a Gaussian fit to the line profile to derive the flux. Otherwise we calculate the line flux using direct integration. If the flux is measured with S/N < 3, we consider the line as undetected and derive a 3σ upper limit. The line flux limit is computed by summing the error spectrum in quadrature over ~200 km s^{-1} (14 Å for a single emission line, and 20 Å for the blended C IV or C III] doublet). This integration range is chosen to be consistent with the upper bound of line widths found for UV metal lines (e.g. Bayliss et al. 2014; James et al. 2014; Stark et al. 2014; Mainali et al. 2017). For each detected line, we calculate the corresponding rest-frame EW. Robust measurements of continuum flux are required to compute EWs. For objects with bright continuum (S/N >5) in the extracted 1D spectra, we derive the flux density in a clean window of ±150 Å near the emission line. For objects lacking confident continuum detection in our spectra, we derive the continuum flux from the best-fitting SED models.

For 24 sources in our $z = 1.3$–3.7 sample (Table 3), we have detected at least one UV metal line (C IV, O III], C III]) with S/N >3. The measured emission line fluxes and EWs are presented in Tables 4 and 5, respectively. In Fig. 4, we show a subset of the sources with UV emission line detections. In most cases, the blended C III] λ1908 doublet is the strongest rest-frame UV emission line (other than Lyα). We measured C III] in 20 extreme [O III] emitters with S/N >3. For three sources in which the spectral region around C III] is contaminated by sky line residuals, we none the less detect emission from O III] λ1666. In the remaining source, we have a detection of the C IV line and a tentative detection (2.4σ) of the C III] emission.

For the 20 galaxies in our sample with C III] detections, the measured fluxes are from 3.1×10^{-18} to 3.2×10^{-17} erg s^{-1} cm^{-2}. We compute the C III] EWs in the range from 1.6 to 18.7 Å, with a median value of 5.8 Å. In comparison, Du et al. (2020) report a similar median C III] EW (4.0 Å) for 33 EELGs at $z \sim 2$ which are selected following similar criteria in T19. Our C III] EWs are also

consistent with the values of $z \sim 2$ EELGs in Stark et al. (2014) (median EW$_{\text{C III}}$ = 7.1 Å) and in Maseda et al. (2017) (median EW$_{\text{C III}}$ = 4.8 Å). On the other hand, investigations of more massive, typical SFGs usually find much lower C III] EWs. The median C III] EW of the individual C III] detections in our sample is ~3–4 times larger than that of SFGs at $z \sim 1$ (median EW$_{\text{C III}}$ = 1.30 Å; Du et al. 2017), $z \sim 2$–3 (median EW$_{\text{C III}}$ = 2.0 Å; Le Fèvre et al. 2019), and $z \sim 3$ (average EW$_{\text{C III}}$ = 1.67 Å derived from composite spectrum; Shapley et al. 2003).

While the 20 C III] emitters in our sample represents a significant boost to the statistics in this very large sSFR regime, the majority of galaxies we observed do not show C III] emission. In many of these cases, the galaxies with non-detections are very faint in the continuum. As a result, our upper limits are often not sufficient to detect C III] or other lines. Indeed, the median 3σ flux limit for galaxies without a C III] detection is 6.6×10^{-18} erg s^{-1} cm^{-2}. Given the range of continuum magnitudes, we calculate a median upper limit of C III] EW =14.8 Å for our sample of non-detected sources. Clearly many of these systems may hold large EW (>5–10 Å) C III] line emission below our detection limits. In the future, we aim to obtain deeper exposures which should allow us to uncover emission lines in many of these galaxies. For the analysis in this paper, we will consider the non-detections when assessing the range of line strengths seen in our sample.

The second most commonly detected UV metal line in our sample is O III] λ1666. Seven galaxies are seen with O III] λ1666 above >3σ (see Tables 4 and 5). The O III] λ1666 EWs range from 2.1 to 6.7 Å with a median value of 4.0 Å. This is larger than the average O III] λ1666 EW (0.23 Å) of typical SFGs at $z \sim 3$ in Shapley et al. (2003) but comparable to the EWs of O III] λ1666 detections in other EELGs at $z \sim 2$ (e.g. Stark et al. 2014; Mainali et al. 2020; Du et al. 2020). The O III] λ1661 emission line is found to be weaker, showing up in only one object, COSMOS-22402 (Fig. 4). The doublet flux ratio in this system is O III] 1666: 1661 = 1.65. For other galaxies in our sample with O III] λ1666 detections, we can place a limit on the O III] doublet ratio of 1666: 1661 > 1.2 at 3σ. This is consistent with both the observed doublet ratios (e.g. Stark et al. 2014; Senchyna et al. 2017; Berg et al. 2019; Mainali et al. 2020) and the ratio computed from theoretical transition probabilities (1666: 1661 $\simeq$ 2.5; Froese Fischer & Saha 1985).

We also detected the Si III] $\lambda\lambda$1883, 1892 emission lines in COSMOS-04064 (Fig. 4). The Si III] EWs (Si III] λ1883 EW = 2.2 ± 0.3 Å, Si III] λ1892 EW = 2.6 ± 0.2 Å) of this object are

Table 3. Coordinates, spectroscopic redshifts, F814W magnitudes, absolute UV magnitudes, UV slopes, dust extinction, [O III]+Hβ EWs, stellar masses, and sSFRs of the 24 galaxies at $z = 1.3$–3.7 with rest-frame UV metal emission line detections (C IV, O III], or C III] detected with S/N >3). Redshifts (z_{spec}) are derived from [O III] λ5007 emission lines, except for COSMOS-16680 whose redshift is derived based on the O III] λ1666 emission line. Dust extinction, stellar masses, and sSFRs are derived from BEAGLE modelling (Section 2.3).

Target	RA	Dec.	z_{spec}	m_{F814W}	M_{UV}	UV slope	$E(B-V)$	$EW_{[O III] + H\beta}$ (Å)	$\log(M_\star/M_\odot)$	sSFR (Gyr^{-1})
COSMOS-04064	10:00:24.375	+02:13:08.921	1.5019	23.50 ± 0.01	-20.57	-2.01	0.12	2192 ± 530	$8.60^{+0.05}_{-0.07}$	61^{+11}_{-6}
COSMOS-04156	10:00:43.037	+02:13:11.174	2.1883	24.49 ± 0.02	-20.52	-2.08	0.06	1389 ± 258	$8.78^{+0.06}_{-0.04}$	45^{+6}_{-7}
COSMOS-04432	10:00:32.201	+02:13:21.399	1.6206	24.86 ± 0.04	-18.91	-1.29	0.33	1608 ± 139	$8.57^{+0.03}_{-0.03}$	614^{+239}_{-190}
COSMOS-04870	10:00:17.219	+02:13:37.980	2.1023	24.65 ± 0.05	-20.04	-1.53	0.16	420 ± 52	$9.21^{+0.08}_{-0.08}$	14^{+7}_{-4}
COSMOS-11530	10:00:28.638	+02:17:48.674	2.0969	24.08 ± 0.01	-20.93	-2.31	0.00	1684 ± 65	$8.19^{+0.01}_{-0.02}$	327^{+14}_{-14}
COSMOS-16680	10:00:48.029	+02:20:57.824	3.1846	24.00 ± 0.02	-21.63	-1.99	0.12	1102 ± 118	$8.94^{+0.14}_{-0.13}$	90^{+35}_{-27}
COSMOS-18358	10:00:40.111	+02:22:00.462	1.6486	23.09 ± 0.02	-21.33	-2.15	0.12	639 ± 37	$9.51^{+0.02}_{-0.03}$	12^{+1}_{-1}
COSMOS-22402	10:00:17.831	+02:24:26.350	2.2751	24.62 ± 0.05	-20.35	-1.79	0.18	682 ± 55	$8.59^{+0.06}_{-0.06}$	107^{+14}_{-13}
COSMOS-24660	10:00:34.285	+02:25:58.495	1.5897	24.84 ± 0.04	-19.39	-1.87	0.15	1050 ± 79	$8.41^{+0.09}_{-0.08}$	43^{+10}_{-9}
UDS-07447	02:17:18.162	-05:15:06.275	1.5972	24.46 ± 0.02	-19.60	-1.61	0.12	983 ± 48	$8.64^{+0.05}_{-0.05}$	25^{+4}_{-3}
UDS-07665	02:17:33.781	-05:15:02.848	2.2955	25.45 ± 0.06	-19.35	-2.18	0.11	1800 ± 127	$8.11^{+0.09}_{-0.08}$	252^{+87}_{-86}
UDS-08735	02:17:34.564	-05:14:48.779	2.2939	25.29 ± 0.05	-18.98	-0.67	0.44	460 ± 24	$10.84^{+0.08}_{-0.09}$	1^{+0}_{-1}
UDS-11010	02:17:14.707	-05:14:20.245	1.6637	26.03 ± 0.08	-19.03	-2.83	0.00	1363 ± 28	$7.62^{+0.06}_{-0.06}$	79^{+10}_{-9}
UDS-11457	02:17:08.085	-05:14:16.134	2.1821	25.04 ± 0.04	-19.89	-1.87	0.12	1572 ± 183	$8.55^{+0.09}_{-0.08}$	148^{+26}_{-36}
UDS-11693	02:17:03.893	-05:14:13.664	2.1854	24.55 ± 0.02	-20.38	-1.82	0.14	869 ± 45	$8.85^{+0.09}_{-0.09}$	35^{+10}_{-8}
UDS-12154	02:17:52.098	-05:14:09.985	2.3065	24.85 ± 0.04	-20.08	-1.50	0.23	689 ± 134	$9.44^{+0.09}_{-0.08}$	6^{+2}_{-2}
UDS-12539	02:17:53.733	-05:14:03.196	1.6211	24.30 ± 0.02	-19.92	-1.97	0.12	1377 ± 44	$8.33^{+0.09}_{-0.06}$	123^{+15}_{-22}
UDS-19167	02:17:43.535	-05:12:43.610	2.1833	24.95 ± 0.03	-20.27	-2.41	0.05	2335 ± 178	$7.95^{+0.02}_{-0.02}$	232^{+15}_{-12}
UDS-21196	02:17:33.633	-05:12:17.791	2.1585	24.13 ± 0.02	-21.08	-2.54	0.01	343 ± 23	$9.17^{+0.04}_{-0.04}$	6^{+1}_{-1}
UDS-27151	02:17:36.141	-05:11:06.180	2.1539	24.33 ± 0.03	-20.68	-2.15	0.10	946 ± 72	$8.80^{+0.10}_{-0.07}$	39^{+9}_{-10}
UDS-29267	02:17:25.322	-05:10:40.397	1.5190	23.85 ± 0.01	-20.71	-2.53	0.00	2787 ± 80	$8.16^{+0.01}_{-0.01}$	316^{+4}_{-3}
UDS-30015	02:17:36.517	-05:10:31.256	1.6649	24.70 ± 0.03	-19.81	-2.06	0.01	1332 ± 73	$7.86^{+0.02}_{-0.02}$	105^{+12}_{-15}
UDS-30274	02:17:21.117	-05:10:28.812	1.4570	23.76 ± 0.02	-20.20	-1.83	0.09	321 ± 28	$9.29^{+0.05}_{-0.06}$	6^{+1}_{-1}
UDS-31649	02:17:06.433	-05:10:13.584	1.4589	23.72 ± 0.01	-20.54	-2.26	0.08	1014 ± 85	$8.96^{+0.04}_{-0.04}$	12^{+1}_{-1}

Table 4. Rest-frame UV metal line fluxes of the 24 sources with one or more UV metal line detections. We provide the 3σ upper limits for non-detections.

Target	z_{spec}	C IV λ1549 ($\times 10^{-18}$ erg s^{-1} cm^{-2})	O III] λ1661 ($\times 10^{-18}$ erg s^{-1} cm^{-2})	O III] λ1666 ($\times 10^{-18}$ erg s^{-1} cm^{-2})	C III] λ1908 ($\times 10^{-18}$ erg s^{-1} cm^{-2})
COSMOS-04064	1.5019	...	...	...	29.99 ± 1.24
COSMOS-04156	2.1883	<5.39	<1.90	<1.87	8.87 ± 0.89
COSMOS-04432	1.6206	...	<4.15	<5.28	17.07 ± 1.44
COSMOS-04870	2.1023	<5.27	<1.59	<1.52	3.15 ± 0.37
COSMOS-11530	2.0969	<6.04	<8.64	7.58 ± 0.89	16.82 ± 1.02
COSMOS-16680	3.1846	...	...	4.28 ± 0.93	...
COSMOS-18358	1.6486	...	<4.54	<4.31	18.62 ± 1.09
COSMOS-22402	2.2751	8.92 ± 1.61	4.26 ± 1.18	7.04 ± 0.96	19.17 ± 1.17
COSMOS-24660	1.5897	...	<5.07	<5.56	6.65 ± 1.61
UDS-07447	1.5972	<18.92	<5.99	<7.21	10.43 ± 2.35
UDS-07665	2.2955	6.19 ± 2.05	<3.95	4.76 ± 1.15	9.32 ± 2.92
UDS-08735	2.2939	25.13 ± 5.74	<3.98	<5.32	9.06 ± 3.83
UDS-11010	1.6637	...	<19.79	<18.77	7.12 ± 1.34
UDS-11457	2.1821	<16.36	<5.56	4.44 ± 1.63	5.40 ± 1.50
UDS-11693	2.1854	<14.73	<6.24	<6.14	5.59 ± 1.56
UDS-12154	2.3065	<12.96	...	5.24 ± 1.44	...
UDS-12539	1.6211	...	<23.77	<22.72	10.12 ± 2.19
UDS-19167	2.1833	8.97 ± 4.50	<6.54	6.95 ± 2.11	...
UDS-21196	2.1585	<17.54	<6.00	<4.55	6.37 ± 1.48
UDS-27151	2.1539	<18.51	<5.11	<7.01	9.93 ± 2.68
UDS-29267	1.5190	...	<7.30	<5.09	31.56 ± 3.72
UDS-30015	1.6649	...	<15.31	<19.36	8.34 ± 1.79
UDS-30274	1.4570	...	...	...	14.03 ± 3.17
UDS-31649	1.4589	...	...	...	6.86 ± 2.15

Table 5. EWs of the rest-frame UV metal emission lines. We provide the 3σ upper limits for non-detections.

Target	$z_{\rm spec}$	C IV $\lambda1549$ (Å)	O III] $\lambda1661$ (Å)	O III] $\lambda1666$ (Å)	C III] $\lambda1908$ (Å)
COSMOS-04064	1.5019	1.5 ± 0.2^{a}	...	1.5 ± 0.3^{a}	7.19 ± 0.30
COSMOS-04156	2.1883	<2.25	<0.91	<0.90	5.60 ± 0.56
COSMOS-04432	1.6206	...	<3.87	<4.93	18.72 ± 1.58
COSMOS-04870	2.1023	<3.03	<1.00	<0.96	2.50 ± 0.30
COSMOS-11530	2.0969	<1.55	<2.61	2.29 ± 0.27	7.01 ± 0.43
COSMOS-16680	3.1846	...	...	2.10 ± 0.46	...
COSMOS-18358	1.6486	...	<0.52	<0.50	2.82 ± 0.16
COSMOS-22402	2.2751	4.68 ± 0.85	2.57 ± 0.71	4.24 ± 0.58	14.54 ± 0.89
COSMOS-24660	1.5897	...	<3.06	<3.35	5.17 ± 1.25
UDS-07447	1.5972	<8.65	<3.07	<3.70	6.58 ± 1.49
UDS-07665	2.2955	8.55 ± 2.83	<3.68	6.73 ± 1.63	17.75 ± 5.56
UDS-08735	2.2939	20.43 ± 4.66	<3.16	<4.22	6.71 ± 2.84
UDS-11010	1.6637	...	<20.72	<19.66	11.55 ± 2.18
UDS-11457	2.1821	<11.32	<4.41	3.53 ± 1.29	5.78 ± 1.61
UDS-11693	2.1854	<8.67	<4.03	<3.96	4.44 ± 1.24
UDS-12154	2.3065	<8.97	...	3.97 ± 1.10	...
UDS-12539	1.6211	...	<11.64	<11.13	5.82 ± 1.26
UDS-19167	2.1833	5.04 ± 2.53	<4.32	4.59 ± 1.39	...
UDS-21196	2.1585	<4.21	<1.73	<1.31	2.60 ± 0.60
UDS-27151	2.1539	<6.27	<2.03	<2.79	5.33 ± 1.44
UDS-29267	1.5190	...	<1.49	<1.04	8.49 ± 1.00
UDS-30015	1.6649	...	<8.41	<10.64	5.77 ± 1.24
UDS-30274	1.4570	...	...	...	4.14 ± 0.94
UDS-31649	1.4589	...	...	...	1.64 ± 0.52

Note. ^{a}From Du et al. (2020).

comparable to those measured for low-mass, metal-poor galaxies at $z \sim 0 - 2$ (Berg et al. 2018, 2019; Mainali et al. 2020). Two systems show Mg II $\lambda\lambda2796$, 2803 emission (see Fig. 4). Both sources show rather intense line emission, with COSMOS-04064 (Mg II $\lambda2796$ EW = 7.5 ± 0.4 Å, Mg II $\lambda2803$ EW = 2.1 ± 0.3 Å) appearing stronger than COSMOS-18358 (Mg II $\lambda2796$ EW = 2.9 ± 0.2 Å, Mg II $\lambda2803$ EW = 2.2 ± 0.2 Å). Since Mg II emission is resonantly scattered by neutral gas, it has been suggested that Mg II line properties may provide a valuable probe of the escape fraction of Lyα photons (e.g. Henry et al. 2018; Feltre et al. 2018). We will discuss the implications of the Mg II strengths in a separate paper.

Nebular He II emission has been seen in both nearby and high-redshift SFGs (e.g. Erb et al. 2010; Shirazi & Brinchmann 2012; Stark et al. 2014; Senchyna et al. 2017; Berg et al. 2018; Senchyna & Stark 2019; Senchyna et al. 2019; Saxena et al. 2020), reflecting a very hard ionizing spectrum. The origin of strong nebular He II $\lambda1640$ and 4686 lines is still a matter of debate, with possibilities including shocks, X-ray binaries, or metal-poor massive stars (e.g. Thuan & Izotov 2005; Senchyna et al. 2017; see also Shirazi & Brinchmann 2012). These papers generally showed that observed He II strengths typically appear larger than predicted by stellar population models, potentially suggesting that these models are missing sources of energetic photons at low metallicity. We detect confident He II $\lambda1640$ emission (8.5σ) in only one galaxy (COSMOS-11530) in our sample. The spectrum of this galaxy also shows O III] $\lambda1666$ and C III] $\lambda1908$ (Fig. 4). The He II EW is 2.2 ± 0.3 Å, comparable to the EWs derived for metal-poor dwarf galaxies at $z \sim 0$–2 (e.g. Erb et al. 2010; Senchyna et al. 2017, 2019; Berg et al. 2019). However, the full width at half maximum (FWHM) of He II (760 km s^{-1}; uncorrected for spectral resolution) is nearly twice that of the O III] $\lambda1666$ emission line (390 km s^{-1} at 5100 Å, i.e. close to the spectral resolution). The broad profile suggests a significant contribution from stellar winds, as is commonly seen in SFGs. Higher spectral resolution is required

to distinguish the nebular and stellar components of He II in this system.

Metal-poor galaxies have also been shown to power nebular C IV emission (e.g. Berg et al. 2016, 2019; Senchyna et al. 2019). We detect the blended C IV $\lambda1549$ doublet with S/N >3 in three galaxies (COSMOS-22402, UDS-07665, and UDS-08735; Fig. 4). The data imply large C IV EWs in COSMOS-22402 (4.7 ± 0.9 Å) and UDS-07665 (8.6 ± 2.8 Å), with C IV/C III] ratios of 0.46–0.66. For UDS-08735, we see even stronger C IV (EW = 20.4 ± 4.7 Å), with a very large C IV/C III] ratio (2.8). We do not see any interstellar or stellar absorption in the vicinity of these lines, but we cannot rule out a modest level of emission line filling (and hence larger C IV line strengths). Higher resolution spectra will provide a more robust measure of the total C IV EWs in these systems. In Section 4.2, we will come back to investigate the ionizing nature of these three systems.

For one of the C III] emitters in our sample (COSMOS-04064), we are not able to constrain rest wavelengths shorter than Si III] due to the low spectral sensitivity at the blue end of IMACS spectra. This galaxy was previously observed with Keck/LRIS in Du et al. (2020), with multiple UV lines detected (C IV $\lambda1549$, He II $\lambda1640$, O III] $\lambda1666$, C III] $\lambda1908$). The C III] EW (6.9 ± 0.3 Å) measured from Du et al. (2020) is consistent with the value measured from our IMACS spectrum (7.2 ± 0.3 Å). When considering this galaxy in the following analysis, we will augment the fluxes and EWs measurements with the fluxes and EWs presented in Du et al. (2020).

3.2 Rest-frame UV spectra at $z \sim 4$–6

The near-infrared spectra of the eleven $z \sim 4$–6 targets described in Section 2.2 allow constraints to be placed on the strengths of rest-frame UV metal lines (O III], C III]). Each MOSFIRE Y-band spectrum is mostly ($\sim$87%) free from strong OH lines. In all but one
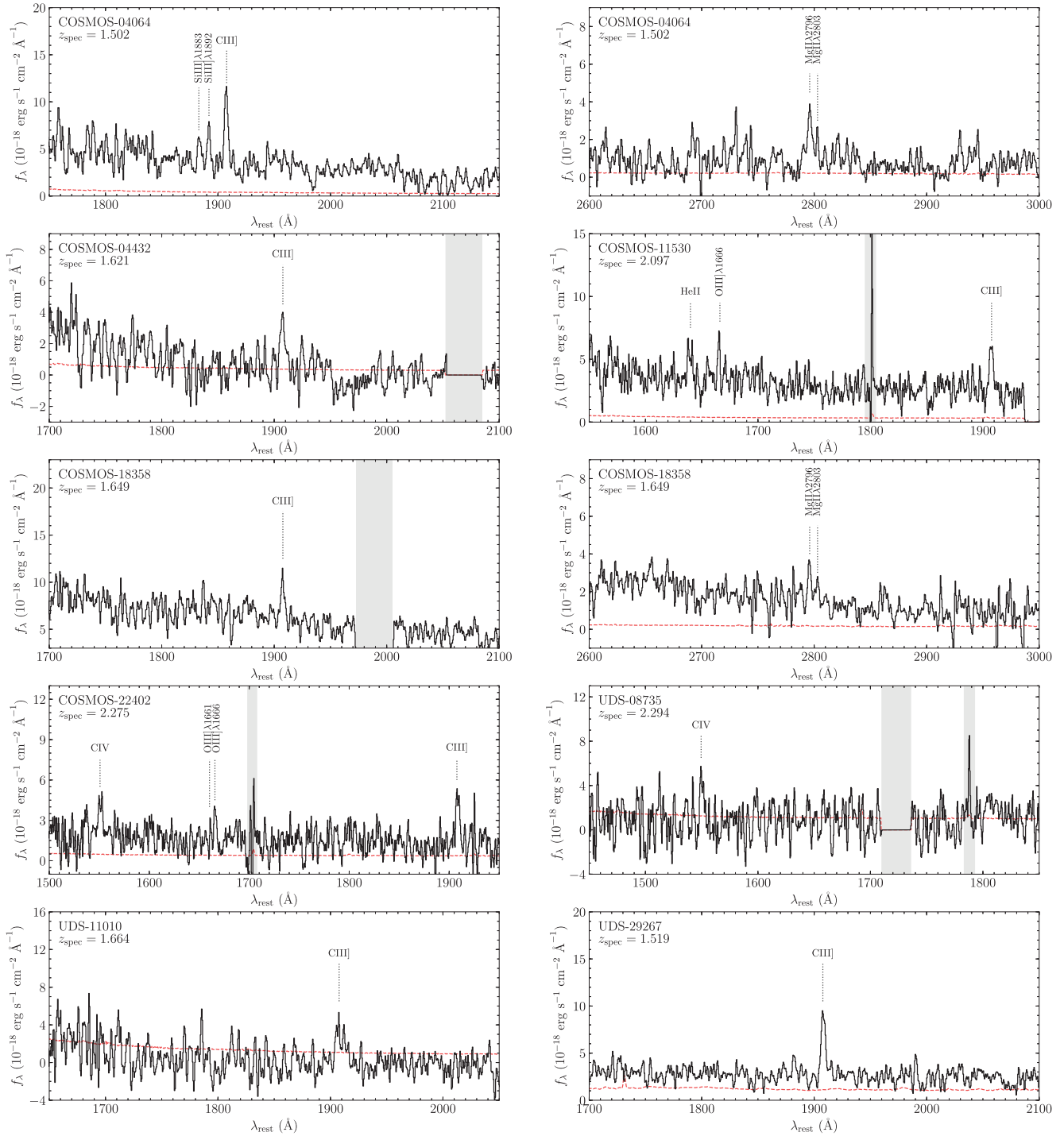
Figure 4. Examples of emission lines detected in the rest-frame UV spectra of $z = 1.3$–3.7 extreme [O III] emitters. The blended C III] $\lambda1908$ doublet is often the most prominent emission line, and we also detected the blended C IV $\lambda1549$, He II $\lambda1640$, O III] $\lambda1661$, 1666, Si III] $\lambda1883$, 1892, and Mg II $\lambda\lambda2796$, 2803 emission lines in a subset of sources. The black solid lines and red dashed lines represent flux and error, respectively. Detected emission lines are marked by black dotted lines. The grey regions indicate gaps between spectra or wavelength ranges contaminated by sky line residuals.

case, the spectra do not show emission lines, so we put upper limits on the UV metal lines. For sources only having photometric redshifts, we report 5σ upper limits. In the one case where the spectroscopic redshift is already known (see Section 2.2), we can more confidently identify faint features because of the narrow wavelength window where the line is expected. For this object, we thus present 3σ upper limits on non-detected lines. To compute constraints on the UV line

EWs, we estimate the underlying broad-band continuum using our best-fitting SED models (Section 2.3). For sources in the redshift range $3.8 < z < 5.0$, the IRAC colour is sensitive to the Hα strength. We quote Hα EWs implied by our photoionization model fits. We summarize the results for each source below and in Table 6.

The GOODS-S mask has six $z > 4$ objects (see Table 2). GOODS-S-46692 is the only galaxy in our sample with a spectroscopic redshift

Table 6. Rest-frame UV metal line constraints on the sources at $z \sim 4$–6. EWs are given in rest frame. For galaxies with spectroscopic redshift measurements, that is, COSMOS-11116 and GOODS-S-46692, the upper limits on line fluxes and EWs are quoted as 3σ. For objects with photometric redshift measurements, the upper limits are quoted as 5σ.

Target	Line	λ_{rest} (Å)	Line flux ($\times 10^{-18}$ erg s^{-1} cm^{-2})	EW$_0$ (Å)
COSMOS-18502	[C III] λ1907	1906.68	<3.1 (5σ)	<4.0 (5σ)
	C III] λ1909	1908.73	<3.1 (5σ)	<4.0 (5σ)
COSMOS-19732	[C III] λ1907	1906.68	<3.0 (5σ)	<2.5 (5σ)
	C III] λ1909	1908.73	<3.0 (5σ)	<2.5 (5σ)
COSMOS-11116	O III] λ1661	1660.81	<1.8 (3σ)	<5.1 (3σ)
	O III] λ1666	1666.15	3.1 ± 0.5	8.8 ± 1.7
COSMOS-15365	O III] λ1661	1660.81	<3.4 (5σ)	<5.2 (5σ)
	O III] λ1666	1666.15	<3.4 (5σ)	<5.2 (5σ)
COSMOS-20187	O III] λ1661	1660.81	<4.3 (5σ)	<22 (5σ)
	O III] λ1666	1666.15	<4.3 (5σ)	<22 (5σ)
GOODS-S-36712	[C III] λ1907	1906.68	<2.4 (5σ)	<6.1 (5σ)
	C III] λ1909	1908.73	<2.4 (5σ)	<6.1 (5σ)
GOODS-S-38450	[C III] λ1907	1906.68	<2.2 (5σ)	<4.9 (5σ)
	C III] λ1909	1908.73	<2.2 (5σ)	<4.9 (5σ)
GOODS-S-39157	[C III] λ1907	1906.68	<2.5 (5σ)	<6.2 (5σ)
	C III] λ1909	1908.73	<2.5 (5σ)	<6.2 (5σ)
GOODS-S-40887	[C III] λ1907	1906.68	<2.6 (5σ)	<9.1 (5σ)
	C III] λ1909	1908.73	<2.6 (5σ)	<9.1 (5σ)
GOODS-S-41253	[C III] λ1907	1906.68	<2.4 (5σ)	<11 (5σ)
	C III] λ1909	1908.73	<2.4 (5σ)	<11 (5σ)
GOODS-S-46692	[C III] λ1907	1906.68	<1.9 (3σ)	<5.5 (3σ)
	C III] λ1909	1908.73	<1.9 (3σ)	<5.5 (3σ)

from earlier efforts (Vanzella et al. 2008), with weak Lyα emission (Lyα EW = 7.7 ± 1.8 Å) indicating a redshift of $z_{Ly\alpha} = 4.811$. The IRAC colour is blue, suggesting the likely presence of strong Hα emission. The BEAGLE SED modelling suggests the IRAC colour can be reproduced with Hα EW = 693 ± 86 Å. In this redshift range, the *Y*-band spectrum covers the C III] doublet. Assuming that the velocity offset of Lyα with respect to C III] is between -200 and 1000 km s^{-1} (e.g. Erb et al. 2014; Stark et al. 2017), the [C III] λ1907 emission line will be located between 11043.5 and 11087.3 Å, and the C III] λ1909 line will be located between 11055.4 and 11099.3 Å. No emission lines are seen in either wavelength range. We note that two OH skylines are located in this wavelength window. However, the wavelength separation of individual emission lines of C III] at this redshift (11.9 Å) guarantees that at least one of the two emission lines should be situated in a clean region of the spectrum. The 3σ upper limit of line flux for each individual component estimated from the clean regions is 1.9×10^{-18} erg s^{-1} cm^{-2}. Here and below, the flux limit is computed by summing the error spectrum in quadrature over ~ 200 km s^{-1} (8 Å), as discussed in Section 3.1 To calculate the upper bound on the C III] EW, we compute the underlying continuum flux using the best-fitting SED model. Taken together with the flux limit, this implies a 3σ upper limit of rest-frame C III] EW = 5.5 Å for each component of the doublet. The measured Lyα line flux of GOODS-S-46692 is 7.43×10^{-18} erg s^{-1} cm^{-2}, and the non-detection of C III] indicates that the flux of doublet is less than 51% of the observed Lyα flux, consistent with the C III]/Lyα ratios observed in $z \simeq 2$ young dwarf galaxies (Stark et al. 2014; Du et al. 2020) and $z > 6$ galaxies (Stark et al. 2015a, 2017).

GOODS-S-41253 ($z_{phot} = 4.28$) has the bluest IRAC [3.6]-[4.5] colour on the GOODS-S mask, consistent with a large Hα EW (829 ± 182 Å). Given its photometric redshift, we expect the C III] $\lambda\lambda$1907, 1909 emission line to lie in the *Y* band. No significant feature (S/N >5) is seen in the spectrum. Using the clean regions

between OH skylines, we estimated the 5σ upper limits of line flux and EW for GOODS-S-41253 are 2.4×10^{-18} erg s^{-1} cm^{-2} and 11 Å. These limits correspond to individual doublet components.

The remaining four objects on the GOODS-S mask are GOODS-S-36712, GOODS-S-38450, GOODS-S-39157, and GOODS-S-40887. These galaxies have smaller flux excesses in the [3.6] filter than the two sources described above, suggesting weaker Hα emission (EW = 200–350 Å). No >5σ feature was found in the MOSFIRE spectra, allowing us to place an upper limit on the C III] line strength. Using the clean regions between OH skylines, we estimated the 5σ upper limits of line flux are $2.2 - 2.6 \times 10^{-18}$ erg s^{-1} cm^{-2}, corresponding to 5σ EW upper limits of 4.9–11 Å for individual components of the doublet.

The COSMOS mask contains five $z \gtrsim 4$ galaxies, two of which (COSMOS-18502 and COSMOS-19732) have IRAC colours indicative of strong Hα emission (400 ± 24 and 1000 ± 101 Å, respectively). Visual inspection of the MOSFIRE spectra reveals no convincing line features. The 5σ upper limit on the line flux between OH skylines is 3.1×10^{-18} erg s^{-1} cm^{-2} for COSMOS-18502 and 3.0×10^{-18} erg s^{-1} cm^{-2} for COSMOS-19732. Using the continuum from the best-fitting SED models, we compute a 5σ EW upper limit (for individual doublet components) of 4.0 Å for COSMOS-18502 and 2.5 Å for COSMOS-19732.

The COSMOS mask additionally contains three objects with photometric redshifts in the range $z = 5.6$–5.8, allowing us to constrain the strength of O III] emission. The first of these sources, COSMOS-11116, has a photometric redshift of $z_{phot} = 5.62$. We detect a 6.2σ emission line feature centred at 11194.3 Å with flux of $3.1 \pm 0.5 \times 10^{-18}$ erg s^{-1} cm^{-2} (Fig. 5), which is at the expected spatial position of COSMOS-11116. The emission line is unresolved, with FWHM similar to the spectral resolution (3.3 Å). It is shown that the emission line has the standard negative–positive–negative pattern resulting from the subtraction of AB dither pattern, indicating that the emission line is present in both dither positions. Given the
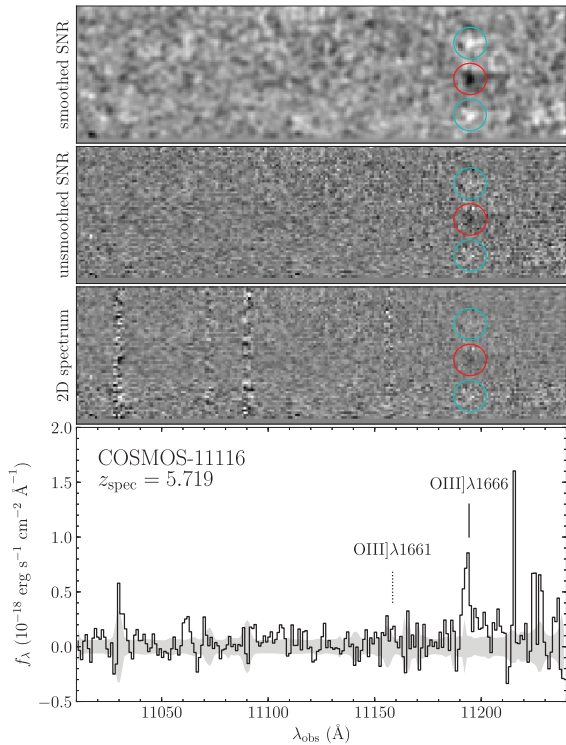
Figure 5. Keck/MOSFIRE *Y*-band spectrum of COSMOS-11116. We identified an emission line feature at 11194.3 Å. This emission line is likely to be O III] λ1666 at $z = 5.719$. The top panel shows the smoothed and unsmoothed 2D S/N map, as well as the 2D spectrum. Red circles show the positive peak of the emission line, while cyan circles show the negative peaks created in dithering. The bottom panel presents the flux-calibrated 1D spectrum, with 1σ error shown in grey. The detected emission line (O III] λ1666 at $z = 5.719$) is marked by the solid black line, and the position where O III] λ1661 (undetected) should be is marked by the dotted black line.

photometric redshift, we conclude that the line is most likely either O III] λ1666 or O III] λ1661. The separation between O III] doublets is $\simeq$ 35 Å at the expected redshift, which is more than 10 times the FWHM of the emission line, indicating that the O III] doublets must be resolved in the spectrum. If the emission line feature is O III] λ1666 (O III] λ1661), the systematic redshift of COSMOS-11116 would be $z = 5.719$ ($z = 5.740$), which is consistent with the photometric redshift. Using the spectroscopic redshift derived from O III] λ1666 (O III] λ1661), we search for O III] λ1661 (O III] λ1666) which should be located at 11158.4 (11230.3) Å. No convincing ($>5\sigma$) emission line feature is detected at the expected position. Theoretical transition probabilities imply a O III] λ1666/O III] λ1661 ratio =2.5 (Froese Fischer & Saha 1985), and the observed doublet ratio found in high-redshift SFGs is 1666: 1661 > 1 (e.g. Stark et al. 2014; Mainali et al. 2020). Therefore, we expect the O III] λ1666 emission line to be stronger than O III] λ1661. As a result, we tentatively identify this emission line as O III] λ1666, implying a spectroscopic redshift of $z = 5.719$. Using the far-UV continuum flux density derived from the best-fitting BEAGLE model, we compute the rest-frame O III] λ1666 EW (=8.8 ± 1.7 Å). For the O III] λ1661 component, we estimate a 3σ upper limit of =1.8 × 10^{-18} erg s^{-1} cm^{-2}. This implies a O III] doublet ratio of 1666: 1661 > 1.7 at 3σ, which is consistent with both the theoretical and observed doublet ratio. The corresponding 3σ upper limit of O III] λ1661 EW is 5.1 Å.

The other two objects we targeted at $z = 5.6$–5.8 are COSMOS-15365 ($z_{\rm phot} = 5.64$) and COSMOS-20187 ($z_{\rm phot} = 5.73$). No

significant ($>5\sigma$) feature is detected in either spectrum. Using the clean regions between OH skylines, we estimate upper limits for the flux and EW of individual components of the O III] doublets. For COSMOS-15365, we derive 5σ upper limits of 3.4 × 10^{-18} erg s^{-1} cm^{-2} and 5.2 Å; whereas for COSMOS-20187, we compute 4.3 × 10^{-18} erg s^{-1} cm^{-2} for the flux limit, and 22 Å for the EW limit.

4 THE PHYSICAL NATURE OF GALAXIES WITH INTENSE REST-FRAME UV NEBULAR EMISSION

We have presented detection of rest-frame UV metal lines in 24 galaxies at $z \simeq 1.3$–3.7 selected to have rest-frame optical line properties similar to those in the reionization era. The emission lines detected in our survey include C III], O III], C IV, Mg II, Si III], and He II, with EWs reaching close to the values seen in sources at $z >$ 6. In this section, we briefly summarize the physical properties of the UV line emitters in our sample (Section 4.1) and then investigate the nature of the ionizing sources responsible for powering the lines, considering whether any of our targets require AGN to explain the observed spectra (Section 4.2).

4.1 Gas conditions and stellar populations

Previous studies have demonstrated that rest-frame UV lines tend to be very prominent in metal-poor low-mass galaxies that are in the midst of a significant star formation episode (e.g. Stark et al. 2014; Feltre, Charlot & Gutkin 2016; Gutkin et al. 2016; Jaskot & Ravindranath 2016; Senchyna et al. 2017, 2019; Plat et al. 2019; Mainali et al. 2020). The BEAGLE photoionization models (Section 2.3) suggest a similar picture for our targets. A summary of inferred properties is listed in Table 3. We have previously described the physical properties of extreme [O III] emitters in our earlier papers (T19, Tang et al., in preparation). Here, we briefly describe the average properties of the 24 galaxies with rest-frame UV line detections below but note that the galaxies are very similar to those from the parent sample. Readers are directed to our earlier papers for more detailed discussion of the implied gas and stellar population properties.

In nearly all of the 24 galaxies with rest-frame UV metal line detections (more on the few exceptions in Section 4.2), models powered by stars are able to reproduce both broad-band data and the observed nebular line detections (see fits in Fig. 2 for examples). The data are best matched by models with low stellar masses (median values of 4.4 × 10^8 M$_\odot$) with gas that has moderately low metallicity and large ionization parameter (medians of $Z = 0.2 Z_\odot$ and log $U = -1.7$). As the UV continuum slopes tend to be very blue (median of $\beta = -2.0$), the best-fitting solutions tend to have minimal reddening from dust (median value of $E(B - V) = 0.12$). The rest-frame optical lines are very intense by virtue of our selection (median of EW$_{\rm [O III] + H\beta} = 1080$ Å), requiring models with large sSFRs (median of 46 Gyr^{-1}) and dominant young stellar populations.

The rest-frame UV emission line spectra (in particular, C III] and C IV) are also sensitive to the C/O ratio of the ionized gas. Previous studies have suggested that for stellar populations to power the most intense C III] emission lines (EW$_{\rm CIII]} > 20$ Å) seen at high redshift, the nebular gas must be enhanced in carbon, with supersolar C/O ratios (Nakajima et al. 2018). While none of our systems are detected above this C III] EW threshold, several are very close. We none the less find that the BEAGLE fits prefer subsolar C/O abundance ratios (0.27 or 0.52 C/O$_\odot$), as the observed C III] flux tends to be overpredicted

in cases where solar C/O ratios are adopted. We can directly test this inference for systems with confident detections of both C III] and O III]. With our current data set, this limits us to COSMOS-11530 and COSMOS-22402, each of which have high quality (S/N >7) measurements of both lines. To infer the C/O ratios, we follow a similar procedure to other recent analyses (e.g. Erb et al. 2010; Stark et al. 2014; Mainali et al. 2020). We first compute the ratio of doubly ionized carbon and oxygen with PYNEB (Luridiana, Morisset & Shaw 2015), using the flux ratios of C III] and O III] together with an estimate of the electron temperature derived from the dust-corrected O III] λ1666/[O III] λ5007 flux ratio. We then apply a small ionization correction factor (ICF) to account for the fact that the fraction of carbon that is in the doubly-ionized state is not necessarily the same as that of oxygen. Following Mainali et al. (2020), we estimate the ICFs using scaling relations derived in Berg et al. (2019). If we conservatively adopt a metallicity range between $0.05\,Z_\odot$ and $0.2\,Z_\odot$, we find ICF values of 1.0 for COSMOS-11530 and 1.4 for COSMOS-22402. Applying these values, we compute C/O ratios of $\log C/O = -0.95 \pm 0.11$ ($0.21 \pm 0.05\,C/O_\odot$) for COSMOS-11530 and $\log C/O = -0.48 \pm 0.13$ ($0.60 \pm 0.18\,C/O_\odot$) for COSMOS-22402. Both values are subsolar, consistent with the range implied by the BEAGLE models.

The spectra and imaging of our targets thus support a picture whereby most of the galaxies in our sample are moderately low-mass and metal-poor systems that have recently experienced a major star formation event. These results are very similar to what has been found in the literature for similar galaxies (e.g. Erb et al. 2010; Stark et al. 2014; Berg et al. 2016, 2019; Vanzella et al. 2016, 2017; Senchyna et al. 2017, 2019), suggesting that the intense UV nebular emission can be explained as a natural byproduct of the hard radiation field associated with very young stellar populations that arise in metal-poor galaxies with significant star formation. In the following section, we consider whether there are any sources in our sample which are unlikley to fit within this framework.

4.2 Ionizing sources

In the last several years, work has focused on the development of rest-frame UV diagnostics that distinguish galaxies with spectra powered by stars from those powered by AGNs (e.g. Feltre et al. 2016; Gutkin et al. 2016; Nakajima et al. 2018). Owing to the presence of several high ionization emission features (C IV, He II), the rest-frame UV is particularly well suited to identify line ratios that require a power-law AGN spectrum in the extreme UV. Here we consider our emission line detections in the context of several of these diagnostics, with the goal of identifying any sources that are not satisfactorily explained with massive stars. This step is a necessary prerequisite for assessing the frequency of low-metallicity stellar populations in galaxies with extreme [O III] emission, while also providing some insight into how common AGN might be in similarly selected samples at $z \gtrsim 6$.

In Fig. 6, we compare our C III] emitting galaxies to the C III] EW versus C III]/He II diagnostic developed by Nakajima et al. (2018). As can be seen in the figure, AGN are generally found with either larger C III] EWs or smaller C III]/He II ratios, the latter reflecting the stronger He II emission that arises from an AGN power-law spectrum. We use this diagnostic primarily because of the data we have available to us at present (our spectral coverage often does not extend to C IV). Note that many of our C III]/He II measurements are lower limits, owing to non-detections of He II. In addition to plotting the line ratios of our sample, we overlay those of AGNs (Hainline et al. 2011) and metal-poor SFGs in the literature (Erb et al. 2010; Stark et al. 2014; Berg et al. 2016, 2019; Senchyna et al.
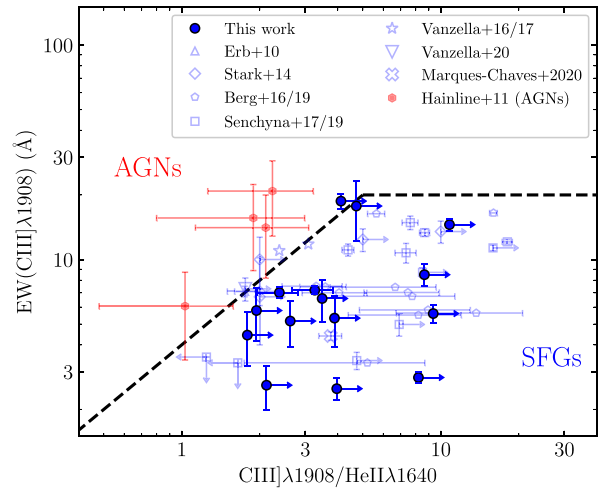

Figure 6. C III] EW versus C III]/He II diagnostic. The black dashed line shows the boundary between AGNs (upper left) and SFGs (lower right). C III] emitters in our sample are presented by blue circles. Blue open symbols show the data of metal-poor SFGs at $z = 0 - 3$ from literature (Erb et al. 2010; Stark et al. 2014; Berg et al. 2016, 2019; Senchyna et al. 2017, 2019; Vanzella et al. 2016, 2017, 2020; Marques-Chaves et al. 2020). Red hexagons show narrow-line AGNs from Hainline et al. (2011).

2017, 2019; Vanzella et al. 2016, 2017). The majority of galaxies in our sample lie in the part of the diagram associated with SFGs in the Nakajima et al. (2018) models. Comparison to the data in the literature gives a similar picture, with the bulk of the sample having either larger C III]/He II ratios ($\gtrsim 2$) or lower C III] EWs than the AGNs in Hainline et al. (2011).

However we note that the two strongest C III] emitters in our sample ($EW_{C III]} = 18.7$ Å for COSMOS-04432 and $EW_{C III]} = 17.8$ Å for UDS-07665) are situated very close to the AGN boundary of the Nakajima et al. (2018) diagnostic. For both sources, the [O III] line is also extremely prominent, with $EW_{[O III] + H\beta} = 1608$ Å (COSMOS-04432) and $EW_{[O III] + H\beta} = 1800$ Å (UDS-07665). These objects thus have nebular line properties that are very similar to what has been seen at $z > 6$, but their position in Fig. 6 suggests that AGN ionization might be required to explain the line ratios. The blended C III] doublets of both sources are narrower ($\Delta v = 253 \pm 20$ km s^{-1}) than the C III] emission seen in type I AGNs (Δv up to ~ 1000 km s^{-1}; Le Fèvre et al. 2019) but similar to typical type II AGNs. While neither source has an X-ray counterpart within a 2.0 arcsec radius, this is consistent with the low X-ray luminosities measured in the C III]-emitting AGNs discussed in Le Fèvre et al. (2019).

The broad-band SEDs offer additional information. The data for UDS-07665 are shown in the upper left panel of Fig. 2. Its UV slope is blue ($\beta = -2.2$) and the near-infrared filters show the characteristic flux excess from strong [O III]+Hβ emission. Such SEDs are very common at $z > 6$ and are consistent with expectations for an unreddened metal-poor galaxy dominated by very young stellar populations. The SED of COSMOS-04432 (top panel of Fig. 7) appears very different. While the flux excess from the rest-frame optical nebular lines are present, the rest-frame UV continuum appears very red ($\beta = -0.90$), likely implying a significant dust covering fraction. Such red UV slopes are very similar to what is often seen in UV-selected $z \simeq 3$ galaxies with narrow-lined AGN (Hainline et al. 2011; Le Fèvre et al. 2019). While rare at $z > 6$, red UV colours are present in a subset of the population with intense [O III] emission (Smit et al. 2018). COSMOS-04432 appears to be an
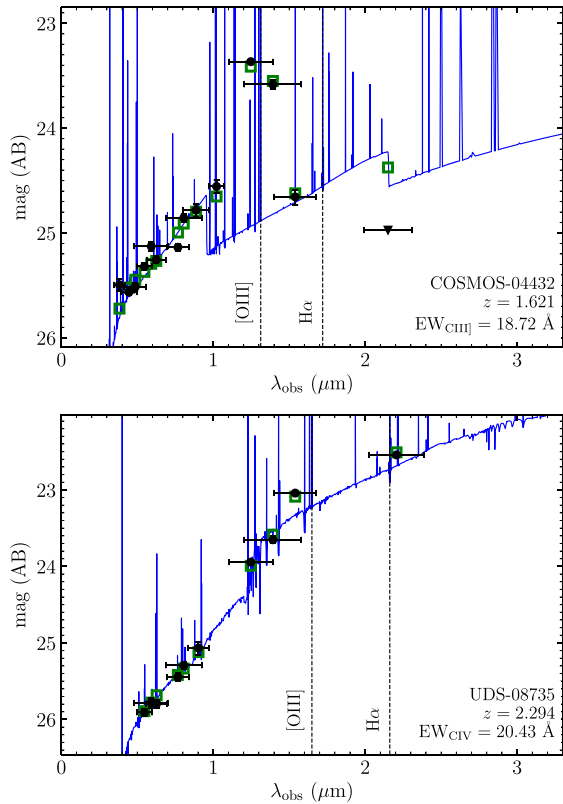
Figure 7. Broad-band SEDs of the two possible AGNs, the extreme C III] emitter COSMOS-04432 (upper panel), and the extreme C IV emitter UDS-08735 (lower panel), both with red UV slopes ($\beta > -1.0$). Observed broadband photometry is shown as solid black circles. The best-fitting SED models inferred from BEAGLE are plotted by solid blue lines, and synthetic photometry is presented by open green squares.

similar instead to the values observed in $z \sim 2$–4 type II quasars (<-0.4, Hainline et al. 2011; Alexandroff et al. 2013). The SED of UDS-08735 (bottom panel of Fig. 7) reveals several additional differences. The UV slope is very red ($\beta = -0.46$), which as we described above is comparable to most AGNs which contaminate SFG samples (Hainline et al. 2011; Le Fèvre et al. 2019). The flux excesses from the rest-frame optical lines are much weaker than in most of our galaxies, reflecting one of the lower [O III]+Hβ EWs in our sample (460 ± 24 Å). If powered by stars, this would indicate a much older stellar population (and hence softer radiation field) than is often linked to strong C IV (e.g. Senchyna et al. 2019). Indeed, the tension in reproducing UDS-08735 with stellar photoionization is readily apparent with BEAGLE. The best-fitting C IV EW ($0.3^{+0.4}_{-0.2}$ Å) is nearly 70 times lower than what is observed. We conclude that this source is most likely an AGN and do not include it in the analysis in the following section.

5 DISCUSSION

Over the last decade, spectroscopic searches have begun to discover a handful of reionization-era analogues with rest-frame UV properties similar to those seen at $z > 6$. In this paper, we have taken steps toward assembling a statistical sample of such systems at $z \simeq 2$–3. Here, we use this data base for two purposes. First, we investigate the C III] EW distribution in galaxies with [O III]+Hβ EW = 1000–2000 Å, with the goal of testing whether the C III] properties seen in the reionization era (C III] EW >15 Å) are uniformly present in low-mass galaxies dominated by extremely young stellar populations (Section 5.1). Second, we quantify the fraction of SFGs in our sample with strong UV line emission, with the goal of constraining how common low-metallicity stellar populations are in low-mass galaxies with large sSFRs at $z \simeq 2 - 3$ (Section 5.2). Both measurements will provide a $z \simeq 2$–3 baseline against which current and future $z > 6$ observations can be compared.

5.1 A baseline for interpreting $z > 7$ C III] detections

Our first goal is geared toward understanding the high EW (>15 Å) C III] detections at $z > 6$. While AGNs have been discovered with similar UV line properties at lower redshifts (Le Fèvre et al. 2019), there are very few examples of SFGs powering comparable spectra, limiting our ability to interpret the nebular emission that has been detected at $z > 6$. Mainali et al. (2020) recently presented discovery of two $z \simeq 2$ gravitationally lensed galaxies with C III] EW $\simeq 15$–20 Å, each of which was selected to have the intense [O III]+Hβ emission ($\simeq 1500$–2000 Å) that is characteristic of galaxies dominated by very young stellar populations. Such systems are extremely rare at lower redshifts, so little is known about the range of rest-frame UV line spectra they exhibit.

Following the survey presented in this paper as well as those in the literature that also satisfy our selection criteria (Mainali et al. 2020; Du et al. 2020), there is now rest-frame UV spectral coverage of C III] for 69 systems with [O III]+Hβ EW >1000 Å, including 12 systems with [O III]+Hβ EW >2000 Å. In Fig. 8, we plot the dependence of C III] EW on the [O III]+Hβ EW for galaxies in our sample and those in the literature. As has been seen previously (e.g. Senchyna et al. 2017, 2019; Maseda et al. 2017; Du et al. 2020), the largest EW C III] emission is seen predominantly at the largest rest-frame optical line EWs. The data in Fig. 8 show that C III] detections with EW >10 Å only begin to be seen in galaxies with [O III]+Hβ EW >500 Å. While such intense optical line emission is relatively rare among massive SFGs at $z \simeq 2$–3 (e.g. Reddy et al. 2018), it becomes the

analogue of these reddened reionization-era sources. Deeper spectra of this low-z analog should reveal detection of the higher ionization lines (C IV, He II) necessary to clarify whether a power-law AGN spectrum is indeed present.

The flux ratio of C IV and O III] provides an additional way to identify sources that may be powered by AGN (e.g. Feltre et al. 2016; Mainali et al. 2017). In particular, the intense radiation field powered by an AGN spectrum triply ionizes a significant fraction of the oxygen, leading to weaker O III] and smaller O III]/C IV flux ratios. Our sample contains five objects with nebular C IV measurements (COSMOS-04064, COSMOS-22402, UDS-07665, UDS-08735, and UDS-19167), none of which show X-ray detections at their positions. Four of the five systems (all but UDS-08735) exhibit line ratios in the range $\log{(\text{O III]/C IV})} = -0.12$ to 0.13, consistent with observations of metal-poor SFGs (e.g. Stark et al. 2014; Berg et al. 2016; Vanzella et al. 2016). The BEAGLE models suggest a similar picture for these four galaxies, with low metallicities ($Z = 0.04 - 0.28\,Z_{\odot}$), young stellar populations (4–26 Myr for constant star formation), and large ionization parameters ($\log U = -1.4$ to -2.2) required to reproduce the full spectra and photometry.

The rest-frame UV spectrum of UDS-08735 is more challenging to reproduce with stars as the primary ionizing source. The C IV EW is the largest in our sample (20.4 ± 4.7 Å), one of the only measurements known with similar values to those seen at $z > 6$. As with the sources described above, no X-ray source is present in the vicinity of the galaxy. However the $\log{(\text{O III]/C IV})}$ ratio (<-0.67 at 3σ) is much lower than in the systems described above,
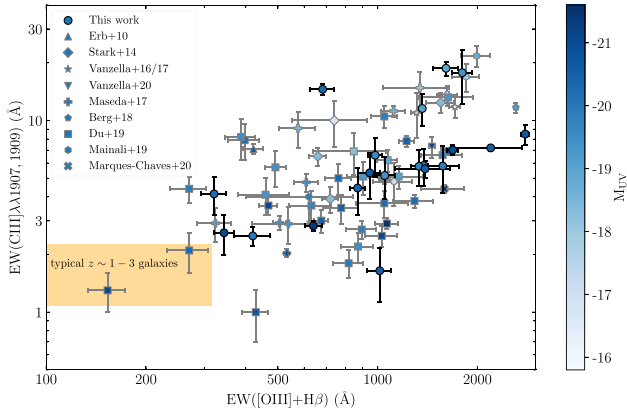
Figure 8. C III] EW as a function of [O III]+Hβ EW for extreme optical line emitters at $z \sim 2$–3, with colour indicating the absolute UV magnitude. Data from objects in our spectroscopic sample are shown as circles. Data from previous investigations of C III] emission in $z \sim 2$–3 galaxies are also included (Erb et al. 2010; Stark et al. 2014; Vanzella et al. 2016, 2017; Maseda et al. 2017; Berg et al. 2018; Vanzella et al. 2020; Mainali et al. 2020; Du et al. 2020; Marques-Chaves et al. 2020). The orange shaded region represents the average and 68% confidence interval of C III] EW (Shapley et al. 2003) and [O III]+Hβ EW (Reddy et al. 2018) of typical, more massive $z \sim 1$–3 galaxies.

norm among galaxies in the reionization era (e.g. Labbé et al. 2013; Smit et al. 2014, 2015; De Barros et al. 2019; Endsley et al. 2020).

We also see in Fig. 8 that the C III] EWs that have been detected in $z > 6$ galaxies (>15–20 Å) appear only at [O III]+Hβ EW >1500 Å in our $z \simeq 2$–3 sample. Given the large sSFR required to power these optical line EWs (T19), this suggests that the C III] lines may be a natural consequence of the hard radiation field associated with extremely young stellar populations (<5–10 Myr). This trend is most clearly seen in the left-hand panel of Fig. 9, where we plot the fraction of galaxies observed in our sample and the literature with C III] EW >15 Å as a function of [O III]+Hβ EW. The C III] emitter

fraction is defined in our analysis as the ratio of sources with C III] EW >15 Å and the total number of galaxies for which we obtained C III] measurements. The latter quantity includes only those non-detections for which we can rule out C III] with EW >15 Å (i.e. we do not include spectra that are too shallow to detect strong emission). Of the 86 galaxies we have observed with sufficient sensitivity at [O III]+Hβ EW = 300–1500 Å, none have been found to exhibit C III] above this threshold. In the 10 galaxies we have targeted with [O III]+Hβ EW >1500 Å, we find one galaxy that has C III] EW >15 Å (here we have excluded COSMOS-04432, the candidate AGN discussed in Section 4.2), implying a fraction of $0.10^{+0.19}_{-0.08}$. Error bars are derived by adopting the statistics from Gehrels (1986). If we include sources in Du et al. (2020) and Mainali et al. (2020), this fraction increases to $0.23^{+0.18}_{-0.12}$. These results suggest that the C III] EWs seen in the reionization era (>15 Å) require very strong optical line emission, becoming somewhat more common in galaxies with [O III]+Hβ EW >1500 Å, similar to previous results at $z \simeq 0$ and $\simeq 2$ (Senchyna et al. 2017; Mainali et al. 2020; Du et al. 2020).

What is perhaps most striking about the results described above is that intense C III] emission is not found to be the norm among the most extreme optical line emitters. Indeed, four of the five galaxies in our [O III]+Hβ EW >1500 Å sample have C III] EW below 10 Å. This includes the most intense line emitter UDS-29267 ([O III]+Hβ EW = 2788 ± 80 Å) in our sample. Based on its optical lines, we naively expected to see among the strongest C III] in our sample. However the spectrum revealed a detection with C III] EW = 8.5 Å, well below the values that have been seen at $z > 6$. Clearly the hard radiation field that emerges from young stellar populations is not a sufficient condition for intense C III] emission.

The BEAGLE photoionization models suggest that the spread in C III] at [O III]+Hβ EW >1500 Å is driven by metallicity. As detailed in Section 2.3, the modelling results are based on fits to the rest-frame UV and optical nebular lines together with the broad-band continuum, and here we focus on those sources with extreme [O III]+Hβ EW (>1500 Å). The results indicate that those galaxies in this subset with strong C III] (11.6–17.8 Å) tend to require lower
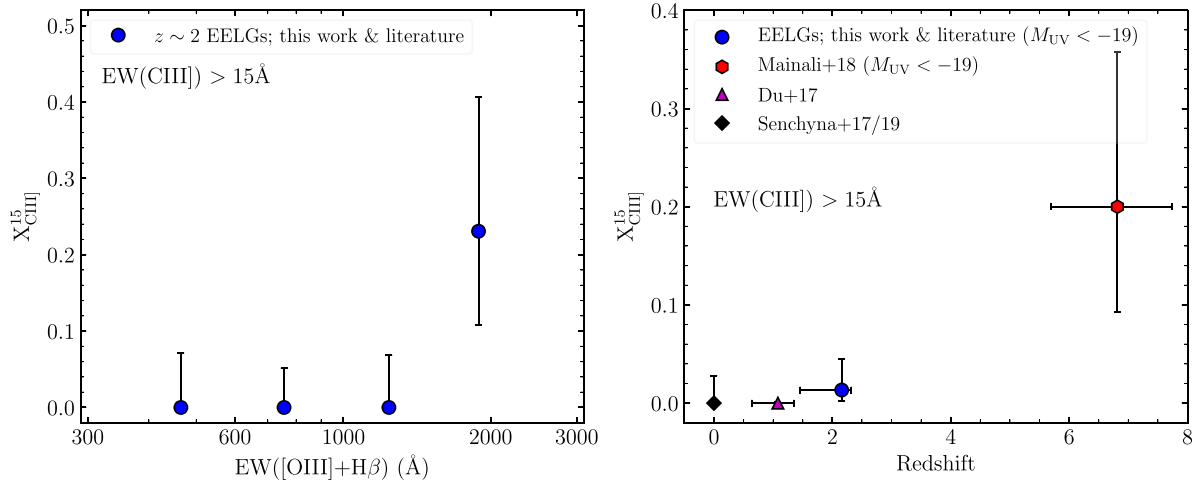

Figure 9. Left-hand panel: fraction of galaxies with extremely large C III] EWs (>15 Å) as a function of [O III]+Hβ EW. We show the C III] fractions for four [O III]+Hβ EW bins (=300–600, 600–1000, 1000–1500, and 1500–3000 Å) for a sample combining our $z = 1.3$–3.7 EELGs and the $z \sim 2$ EELGs in Du et al. (2020) and Mainali et al. (2020). Right-hand panel: fraction of galaxies with C III] EW >15 Å as a function of redshift. The fraction at $z \sim 0$ (black diamond) and $z \sim 1$ (magenta triangle) are derived from Senchyna et al. (2017, 2019) and Du et al. (2017). The $z = 5.4$ data (red hexagon) is computed using the spectroscopic sample from literature, which are summarized in Mainali et al. (2018) and add the newly detected C III] in a $z = 7.5$ galaxy (Hutchison et al. 2019). The fractions of extreme C III] emitter at $z \sim 2$ in EELGs (combining our sample and those in Du et al. 2020 and Mainali et al. 2020; blue circle) are constrained to objects with [O III]+Hβ EW = 300–3000 Å and $M_{UV} < -19$, which are comparable to the values of extreme C III] emitters at $z > 5.4$.
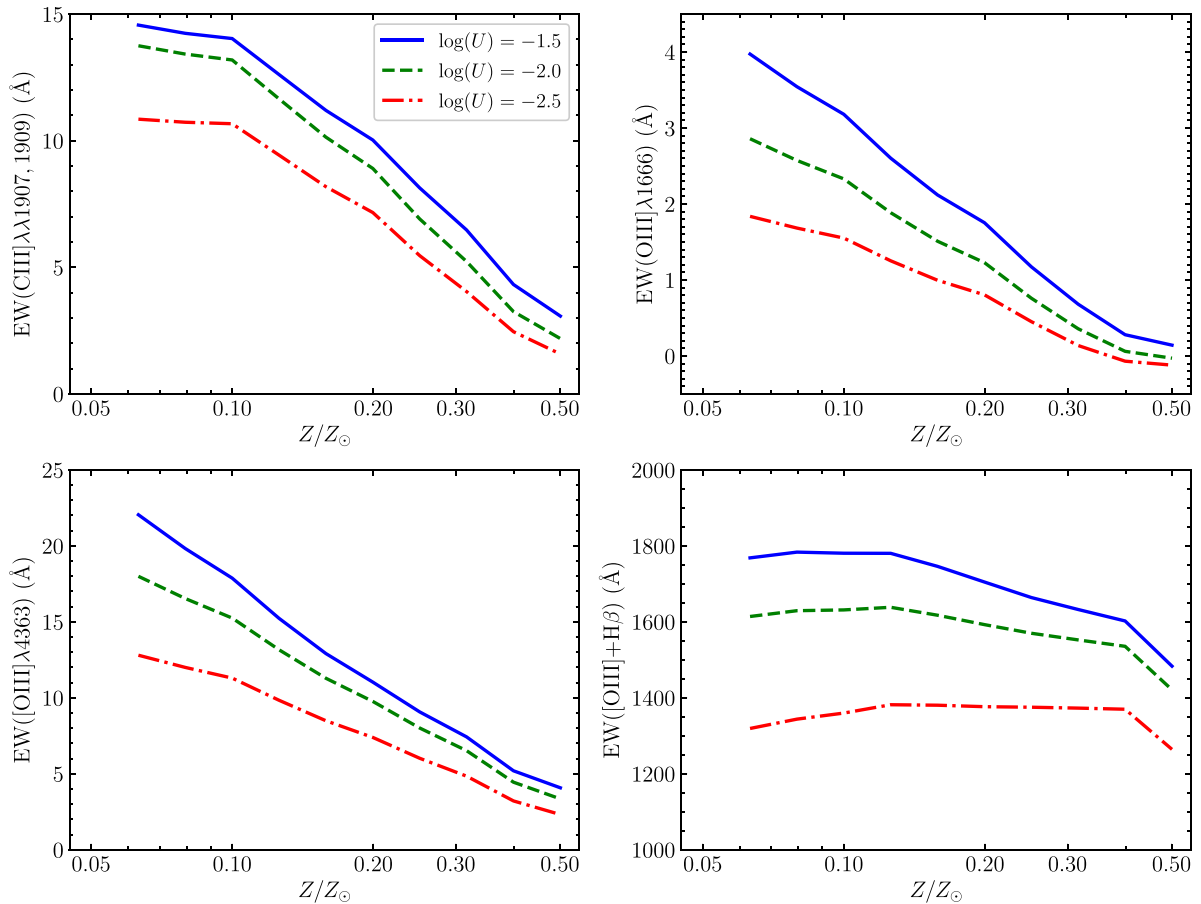
Figure 10. Predicted C III] λλ1907, 1909 EW (upper left), O III] λ1666 EW (upper right), [O III] λ4363 EW (lower left), and [O III]+Hβ EW (lower right) from BEAGLE models for different metallicities at age =10 Myr (assuming constant star formation history). Models with different ionization parameters are shown by red dashed–dotted lines (log $U = -2.5$), green dashed lines (log $U = -2.0$), and blue solid lines (log $U = -1.5$).

metallicities (median of $0.07\,Z_\odot$), whereas those with weaker C III] (5.8–7.2 Å) are fitted with more moderate metallicities (median of $0.28\,Z_\odot$). The strong and weak C III] emitters are found to have nearly identical ionization parameters (median of log $U = -1.71$ and -1.68, respectively) and fairly similar sSFRs (median of 79 and 129 Gyr^{-1}). Both subsets prefer subsolar C/O ratios (0.52 C/O$_\odot$), and deviations from this lead to tension with the observed C III] strength. The photoionization models thus suggest that metallicity is the primary driver of the spread in C III] at fixed [O III] EW. More work is needed to confirm this trend with the temperature-sensitive auroral lines. For the few existing cases in which high S/N auroral line detections exist, the direct-method metallicities confirm the presence of low metallicities ($\simeq 10\%\,Z_\odot$) in the most extreme C III] emitters (see e.g. Mainali et al. 2020).

The luminosity distribution of our galaxies suggests a similar picture, with the strength of C III] emission (at fixed [O III]+Hβ EW) generally increasing toward lower luminosities (see colour bar in Fig. 8) where low-metallicity gas and stars are more likely. To investigate the dependence of C III] on UV luminosity, we quantify the average C III] EW in bins of $M_{\rm UV}$ for galaxies with extreme [O III]+Hβ emission (EW > 1500 Å), including those in our sample and those in the literature selected similarly (Mainali et al. 2020; Du et al. 2020). To avoid biasing our results, we only consider those spectra with the sensitivity to detect weak C III] emission (EW = 5 Å). As we will discuss below, this limits our sample of lower luminosity galaxies where continuum magnitudes are faint. Focusing first on

luminous galaxies ($M_{\rm UV} < -19.5$), there are four [O III]+Hβ EW >1500 Å systems in our sample with deep C III] constraints. Of these, none have C III] EW >10 Å, and the median value is just C III] EW = 6.5 Å. At lower luminosities ($M_{\rm UV} > -19.5$), there are only three [O III]+Hβ EW >1500 Å galaxies with deep enough spectra to detect weak C III], allowing a fair comparison with our bright sample. Two of these are from Mainali et al. (2020) and the third is from Du et al. (2020). Notably, all three have C III] EW >10 Å, with a median value of C III] EW = 16.9 Å. While samples are admittedly small, these results suggest that at $z \simeq 2$–3, the strongest C III] emission (EW >10 Å) is found primarily in low-luminosity galaxies.

The role of metallicity in regulating C III] has been pointed out elsewhere (Erb et al. 2010; Stark et al. 2014; Rigby et al. 2015; Jaskot & Ravindranath 2016; Senchyna et al. 2017; Byler et al. 2018; Plat et al. 2019; Du et al. 2020; Ravindranath et al. 2020), reflecting increased collisional excitation in higher temperature gas and the harder radiation field associated with metal-poor massive stars. But what is perhaps surprising about our results is that C III] appears to react more to a change in metallicity than [O III] over the range considered here (0.1–0.3 $Z_\odot$). This can be seen more clearly in Fig. 10, where we plot the dependence of the C III] EW on metallicity in BEAGLE at fixed stellar age (10 Myr, assuming constant star formation history) and fixed ionization parameter. Since ionization parameter is well known to anticorrelate with metallicity, we show the trend for three ionization parameters (log $U = -2.5$, -2.0, and -1.5). We also display the same trends for two temperature-sensitive

auroral lines (O III] λ1666 and [O III] λ4363) and for the [O III]+Hβ optical lines. Between 0.3 and 0.1 $Z_\odot$, we see that the C III] EW increases by roughly a factor of two (at fixed log U). This closely tracks the rise seen in both auroral lines, suggesting that C III] is very sensitive to the gas temperature in this metallicity regime. In contrast, the [O III]+Hβ EW remains nearly constant over the metallicity range. Even accounting for the larger ionization parameters expected at lower metallicity (log $U = -2.0$ at 0.1 $Z_\odot$ and log $U = -2.5$ at 0.3 $Z_\odot$ according to Pérez-Montero 2014; Sanders et al. 2020), the BEAGLE models predict that the [O III]+Hβ EW will only increase by a factor of 1.1 times over this metallicity range. While this is computed for stellar ages of 10 Myr, we find similar results for older age populations. A similar picture was previously discussed in Jaskot & Ravindranath (2016, see their fig. 9). Because we are plotting equivalent width, the trend seen in Fig. 10 is sensitive to how the underlying continuum varies with metallicity. Since bluer colours are produced by lower metallicity stellar populations, we expect a slight decline in optical EWs with respect to those seen in the UV as we look toward lower metallicities. However, we have verified using BEAGLE that the trends seen in Fig. 10 remain when considering only line luminosity (see also Jaskot & Ravindranath 2016), suggesting that continuum is not a dominant factor.

The physical explanation for the divergent metallicity trends of the C III] and [O III] luminosities is straightforward and has been suggested previously in Plat et al. (2019). The emissivity of both lines is proportional to the collisional excitation rate, which in turn depends on the ionized gas temperature and the energy of the excited state as $T^{-1/2}e^{-E/kT}$. For C III] λλ1907, 1909, the excited state has an energy of $E/k = 7.6 \times 10^4$ K, while for [O III] λλ4959, 5007, the energy is just $E/k = 2.9 \times 10^4$ K. It is straightforward to see that as the gas temperature increases from 1.0 to 1.5×10^4 K, the emissivity of C III] increases considerably more than that of [O III]. The two auroral lines shown in Fig. 10 have excited states with energies similar to that of C III] ($E/k = 8.7 \times 10^4$ K for O III] λ1666 and $E/k = 6.2 \times 10^4$ K for [O III] λ4363), leading to a similar trend with metallicity. These results suggest that as we approach the metallicity range of 0.1–0.3 $Z_\odot$ (an important regime at $z > 6$; e.g. Jones et al. 2020), the collisionally excited UV lines will play an increasingly important role in cooling owing to the higher energies of their excited states (Plat et al. 2019) and as a result, should be increasingly prominent in deep rest-frame UV spectra. It is conceivable that early galaxies will be significantly enhanced in oxygen relative to iron (e.g. Steidel et al. 2016; Strom et al. 2018; Sanders et al. 2020; Jeong et al. 2020; Topping et al. 2020), leading to a harder ionizing spectrum and potentially stronger nebular emission. Following the same photoionization modelling approach as Topping et al. (2020), we find that variations in stellar metallicity at a given gas-phase metallicity do not significantly change the strength of C III] at fixed [O III] EW. The dispersion in C III] at a given [O III] EW appears to be dominated by the variations in gas-phase metallicity described above.

The results laid out above have implications for our understanding of the C III] detections at $z > 7$ (Stark et al. 2017; Hutchison et al. 2019). In addition to having extremely strong C III] (EW >16–22 Å), these galaxies are found to be quite luminous ($M_{UV} = -22.1$ and -21.6). As we outlined above, at $z \simeq 2$–3, very strong C III] is primarily seen among lower luminosity ($M_{UV} > -19.5$) galaxies, as it is in these systems where the metal-poor gas required to support such intense emission is more likely to be found. The presence of strong C III] emission in luminous galaxies at $z \simeq 7$–8 may be one of the first hints of evolution in the luminosity–metallicity relationship between $z \simeq 2$–3 and $\simeq 7$, with lower metallicities at fixed M_{UV} in

the reionization-era population. Current sensitivity limits at $z \simeq 7$ allow us to detect C III] only in galaxies with extreme [O III]+Hβ emission, so these inferences are valid only for the subset of the population with very large sSFR. The emergence of new samples of bright galaxies at $z \simeq 7$ with intense optical line emission (e.g. Endsley et al. 2020) should allow improved statistics on the C III] EW distribution in this extreme population in the near future.

5.2 Redshift evolution of UV line fractions

The results presented in this paper allow us to revisit the redshift evolution of the fraction of galaxies with intense (EW >15 Å) C III] emission (right-hand panel of Fig. 9). Here we have updated the $z >$ 5.4 data point from Mainali et al. (2018) to include the new detection presented in Hutchison et al. (2019) and reconsider the measurement at $z \simeq 2$–3 (see below). While statistics are still limited, it is clear that the fraction of galaxies with strong C III] (EW >15 Å) at $z >$ 5.4 ($0.20^{+0.16}_{-0.11}$) is larger than in samples at lower redshift. Some of this evolution can be explained by recent results which demonstrate the emergence of a significant population of extreme sSFR galaxies (>200 Gyr^{-1}) with [O III]+Hβ EW >1500 Å at $z > 6$ (De Barros et al. 2019; Endsley et al. 2020), as it is only above these large optical line EWs where intense C III] emission becomes common in SFGs (e.g. left-hand panel of Fig. 9).

However if the evolution toward larger [O III]+Hβ EWs is the entire explanation for the rise in the frequency of detecting intense C III] emission, then we would expect the C III] fraction in our sample of $z \simeq 2$–3 EELGs to be similar to that seen in the reionization era. To test this, we have attempted to construct a sample that is matched in [O III]+Hβ EW to that in the $z > 5.4$ sample. We include galaxies with [O III]+Hβ EW = 300–3000 Å and $M_{UV} < -19$, including our sample (46 sources) together the [O III]-selected samples that satisfy these criteria in Du et al. (2020, 28 sources) and Mainali et al. (2020, 1 source). The median [O III]+Hβ EW in this sample is 760 Å, similar to that in samples at $z \simeq 7$–8 (Labbé et al. 2013; De Barros et al. 2019; Endsley et al. 2020). Of the 75 galaxies that satisfy these criteria, only 1 has C III] EW >15 Å. This implies a fraction of $0.013^{+0.031}_{-0.011}$, much lower than seen at $z > 5.4$. While the uncertainties at $z > 5.4$ remain sizeable, this suggests that the emergence of extreme sSFR systems at $z \simeq 7$ (Endsley et al. 2020) is not enough on its own to drive the large C III] emission we have observed in early galaxies. As described in Section 5.1, we suggest that this may additionally reflect evolution toward lower metallicities at earlier times. Indeed, if the luminous galaxy population evolves from 0.5 to 0.1 $Z_\odot$ between $z \simeq 2$ and $z \simeq 7$, we would expect to see a significant rise (up to 5 times) in C III] EWs without any evolution in sSFR (Fig. 10). We thus suggest that the combination of larger sSFRs and lower metallicities likely work together to explain the large C III] EWs that are being observed at $z > 6$.

Finally, we compare the fraction of star-forming sources in our $z \simeq$ 2–3 sample with nebular C IV emission to that seen at $z > 6$. Since powering C IV requires a hard ionizing spectrum associated with very low-metallicity stars (< 0.1 $Z_\odot$), this comparison will allow us to investigate evolution in the incidence of very low-metallicity stellar populations among galaxies with extreme optical line emission. The first step is to assemble the statistical baseline at $z \simeq 2$–3. Here we consider objects with large [O III]+Hβ EWs (=1000–3000 Å) and $M_{UV} < -19$, focusing on galaxies at $z = 1.7$–3, where C IV is visible from the optical spectrographs we have used. Taking together our sample and the extreme [O III] emitter sample in Du et al. (2020, and removing the AGN candidate discussed in Section 4.2), we find that only 2 out of 21 sources at $z \sim 2$–3 show C IV EW >5 Å,

and none of them shows C IV EW >10 Å. For very low-metallicity systems, we might begin to see weaker [O III] emission, so we also consider galaxies with [O III]+Hβ EW = 500–1000 Å. Here, there are another 23 objects from both our sample and that of Du et al. (2020) that have deep C IV constraints, but none show detections of C IV with EW >5 Å.

These results stand in sharp contrast to the two C IV detections at $z > 6$, both of which show EW >20 Å in $z > 6$ galaxies with $M_{UV} = -20$ to -19 (Stark et al. 2015b; Mainali et al. 2017; Schmidt et al. 2017). The absence of such line emission in similar luminosity systems at $z \simeq 2$–3 is suggestive of a shift toward some combination of harder ionizing spectra and weaker underlying UV continuum in a subset of $z > 6$ galaxies. Since we are considering samples of similar optical line EW (and similar sSFR), this cannot simply be explained by evolution towards galaxies dominated by younger stellar population (i.e. larger [O III]+Hβ EW). Instead, this likely implies the emergence of massive-star populations dominated by very low metallicities at early times. Ultimately larger data sets at $z > 6$ will present a clearer picture of the C IV EW distribution in the reionization era and the physical cause of any evolution that is present. Statistical samples at $z \simeq 2$–3 will continue to be critical in the interpretation of this population.

6 SUMMARY

We have presented rest-frame UV spectroscopic observations of 138 galaxies with extreme [O III]+Hβ line emission at $z = 1.3$–3.7 and 11 sources at $z \sim 4$–6. The galaxies have rest-frame [O III]+Hβ EWs =300–3000 Å, similar to the EWs of galaxies in the reionization era (e.g. Labbé et al. 2013; Smit et al. 2015; Endsley et al. 2020). The data set allows us to measure the C III] $\lambda\lambda$1907, 1909 and C IV $\lambda\lambda$1548, 1550 emission lines, which are found to be intense (EW >15–20 Å) in $z > 6$ galaxies (Stark et al. 2015a, b, 2017; Mainali et al. 2017; Hutchison et al. 2019). Using this statistical sample of reionization-era analogues at $z \simeq 1$–3, we aimed to interpret the nebular line emission emerging at $z > 6$ with two goals. First, we investigated the C III] EW distribution in galaxies with [O III]+Hβ EW >1000–2000 Å, to see whether the EW >15 Å C III] line emission are uniformly present in these systems. Second, we sought to constrain the fraction of strong UV line emitters in our sample of large sSFR galaxies, providing a baseline at $z \simeq 1$–3 to compare with future observations at $z > 6$. We summarize our findings below:

(1) We detect rest-frame UV emission lines (C IV $\lambda\lambda$1548, 1550, He II λ1640, O III] $\lambda\lambda$1661, 1666, Si III] $\lambda\lambda$1883, 1892, C III] $\lambda\lambda$1907, 1909, or Mg II $\lambda\lambda$2796, 2803) in 24 extreme [O III] emitters at $z = 1.3$–3.7 in our sample using Magellan/IMACS and MMT/Binospec. Four objects show C IV emission lines (EW = 1.5–20.4 Å) with S/N >3, with one of the C IV detections coming from Du et al. (2020). The blended C III] doublet has been detected in 20 sources, with EW = 1.6–18.7 Å and a median value of 5.8 Å. The C III] EWs measured in our sample are consistent with those of $z \sim 2$ EELGs in the literature (Stark et al. 2014; Maseda et al. 2017; Du et al. 2020), and are ∼4 times larger than those of more massive, typical SFGs at $z \sim 1$–3 (e.g. Shapley et al. 2003; Du et al. 2017). The largest C IV and C III] EWs ($\simeq 20$ Å) found in our $z = 1.3$–3.7 sample are comparable to that found at $z > 6$.

(2) We find that for all but one of the 24 galaxies with UV metal line detections at $z = 1.3$–3.7, the nebular emission lines and broadband photometry can be reproduced by photoionization models powered by stars. The models suggest these systems are characterized by low stellar masses (median $M_\star = 4.4 \times 10^8\ M_\odot$), little dust reddening (median $E(B - V) = 0.12$), large ionization parameters (median log $U = -1.7$), and low metallicities (median $Z = 0.2 Z_\odot$). Both the observed C III]/O III] ratios and photoionization models imply subsolar carbon-to-oxygen ratios (C/O $\simeq 0.2$–0.5 C/O$_\odot$). The large [O III]+Hβ EWs (median value of 1080 Å) indicate very large sSFRs (median =46 Gyr^{-1}), suggesting an ionizing spectrum dominated by very young stellar populations.

(3) We explore the relationship between C III] EW and [O III]+Hβ EW for galaxies at $z \simeq 1$–3. The intense C III] line emission detected at $z > 6$ (EW >15 Å) only appears in galaxies with the largest [O III]+Hβ EWs (>1500 Å), suggesting that very large sSFR ($\gtrsim 100$ Gyr^{-1}) is required to power the line emission seen at $z > 6$. We find that there is significant variation in C III] EW at fixed [O III]+Hβ EW, with many of the most extreme optical line emitters showing relatively weak C III] emission (EW <8 Å).

(4) Photoionization models suggest that the spread in C III] is driven by metallicity variations at fixed [O III]+Hβ EW, a result of the extreme sensitivity of C III] to electron temperature. We find that strong C III] emission (EW >15 Å) tends to be found in low-metallicity galaxies ($\simeq 0.1 Z_\odot$) with large sSFR, and weaker C III] (EW = 5–8 Å) tends to be found in moderate-metallicity systems ($\simeq 0.3 Z_\odot$) with large sSFR. The luminosity distribution supports this picture, with strong C III] emission generally associated with the lowest luminosity ($M_{UV} > -19.5$) galaxies at a given [O III]+Hβ EW, where low metallicities are most likely. Among more luminous galaxies at $z \simeq 2$–3 ($M_{UV} < -19.5$), we tend to find weaker C III] emission. These results stand in contrast to those at $z > 7$, where very strong C III] has already been identified in extremely luminous ($M_{UV} \simeq -22$) galaxies (Stark et al. 2017), suggesting very low-metallicity gas in some of the most massive galaxies known at $z > 7$. While larger samples are ultimately required to confirm, this is consistent with expectations for evolution toward lower metallicities (at fixed luminosity) between $z \simeq 2$–3 and $\simeq 7$.

(5) We compute the fraction of $z \simeq 2$–3 galaxies with intense C III] emission (EW >15 Å), considering sources that are bright ($M_{UV} < -19$) and have large [O III]+Hβ EWs (300–3000 Å; median =760 Å) as have been targeted spectroscopically in the reionization era. Even when we consider the most extreme [O III] emitting galaxies, we find that a very small fraction of galaxies exhibit intense C III] emission ($0.013^{+0.031}_{-0.011}$), much lower than the fraction that is inferred at $z > 5.4$ (0.20; Mainali et al. 2018; Hutchison et al. 2019). This suggests that the intense C III] emission seen at $z > 6$ is not entirely driven by a shift toward younger stellar populations (i.e. larger [O III]+Hβ EW) and that evolution toward lower metallicities is also likely contributing to the detection rate.

(6) We quantify the fraction of extreme [O III] emitters with nebular C IV emission in our sample, providing a window on the presence of very low-metallicity stellar populations ($< 0.1 Z_\odot$) at $z \simeq 2$–3. Considering those systems in our sample with [O III]+Hβ EW = 1000–3000 Å and $M_{UV} < -19$, we find that only 2 out of 21 sources show C IV EW >5 Å and none of them shows C IV EW >10 Å. To account for the possibility that [O III] may be weaker at such low metallicities, we also consider another 23 galaxies with [O III]+Hβ EW = 500–1000. None shows C IV with EW >5 Å. These results stand in contrast to the detection of C IV with EW >20 Å in two of the first $z > 6$ galaxies targeted with $M_{UV} < -19$ (Stark et al. 2015b; Mainali et al. 2017; Schmidt et al. 2017). The emergence of such strong C IV emission may reflect the increased incidence of very low-metallicity stars ($< 0.1 Z_\odot$) in the reionization-era population.

DATA AVAILABILITY

The data underlying this article will be shared on reasonable request to the corresponding author.

REFERENCES

Alexandroff R. et al., 2013, MNRAS, 435, 3306
Amorín R. et al., 2017, Nat. Astron., 1, 0052
Atek H. et al., 2011, ApJ, 743, 121
Atek H., Richard J., Kneib J.-P., Schaerer D., 2018, MNRAS, 479, 5184
Bayliss M. B., Rigby J. R., Sharon K., Wuyts E., Florian M., Gladders M. D., Johnson T., Oguri M., 2014, ApJ, 790, 144
Berg D. A., Skillman E. D., Henry R. B. C., Erb D. K., Carigi L., 2016, ApJ, 827, 126
Berg D. A., Erb D. K., Auger M. W., Pettini M., Brammer G. B., 2018, ApJ, 859, 164
Berg D. A., Erb D. K., Henry R. B. C., Skillman E. D., McQuinn K. B. W., 2019, ApJ, 874, 93
Bouwens R. J. et al., 2015, ApJ, 803, 34
Brammer G. B., van Dokkum P. G., Coppi P., 2008, ApJ, 686, 1503
Bressan A., Marigo P., Girardi L., Salasnich B., Dal Cero C., Rubele S., Nanni A., 2012, MNRAS, 427, 127
Bruzual G., Charlot S., 2003, MNRAS, 344, 1000
Byler N., Dalcanton J. J., Conroy C., Johnson B. D., Levesque E. M., Berg D. A., 2018, ApJ, 863, 14
Caffau E., Ludwig H. G., Steffen M., Freytag B., Bonifacio P., 2011, Sol. Phys., 268, 255
Calzetti D., Armus L., Bohlin R. C., Kinney A. L., Koornneef J., Storchi-Bergmann T., 2000, ApJ, 533, 682
Chabrier G., 2003, PASP, 115, 763
Chen Y., Bressan A., Girardi L., Marigo P., Kong X., Lanza A., 2015, MNRAS, 452, 1068
Chevallard J. et al., 2018, MNRAS, 479, 3264
Chevallard J., Charlot S., 2016, MNRAS, 462, 1415
Dayal P., Ferrara A., 2018, Phys. Rep., 780, 1
De Barros S. et al., 2016, A&A, 585, A51
De Barros S., Oesch P. A., Labbé I., Stefanon M., González V., Smit R., Bouwens R. J., Illingworth G. D., 2019, MNRAS, 489, 2355
Dressler A. et al., 2011, PASP, 123, 288
Du X., Shapley A. E., Martin C. L., Coil A. L., 2017, ApJ, 838, 63
Du X., Shapley A. E., Tang M., Stark D. P., Martin C. L., Mobasher B., Topping M. W., Chevallard J., 2020, ApJ, 890, 65
Endsley R., Stark D. P., Chevallard J., Charlot S., 2020, MNRAS, Available at: https://doi.org/10.1093/mnras/staa3370
Erb D. K. et al., 2014, ApJ, 795, 33
Erb D. K., Pettini M., Shapley A. E., Steidel C. C., Law D. R., Reddy N. A., 2010, ApJ, 719, 1168
Fabricant D. et al., 2019, PASP, 131, 075004
Feltre A. et al., 2018, A&A, 617, A62
Feltre A. et al., 2020, A&A, 641, A118
Feltre A., Charlot S., Gutkin J., 2016, MNRAS, 456, 3354
Ferland G. J. et al., 2013, RMxAA, 49, 137
Finkelstein S. L. et al., 2015, ApJ, 810, 71
Froese Fischer C., Saha H. P., 1985, Phys. Scr, 32, 181
Gehrels N., 1986, ApJ, 303, 336
Gutkin J., Charlot S., Bruzual G., 2016, MNRAS, 462, 1757
Hainline K. N., Shapley A. E., Greene J. E., Steidel C. C., 2011, ApJ, 733, 31
Henry A., Berg D. A., Scarlata C., Verhamme A., Erb D., 2018, ApJ, 855, 96
Hutchison T. A. et al., 2019, ApJ, 879, 70
Inoue A. K., Shimizu I., Iwata I., Tanaka M., 2014, MNRAS, 442, 1805
James B. L. et al., 2014, MNRAS, 440, 1794
Jaskot A. E., Ravindranath S., 2016, ApJ, 833, 136
Jeong M.-S. et al., 2020, ApJ, 902, L16
Jones T., Sanders R., Roberts-Borsani G., Ellis R. S., Laporte N., Treu T., Harikane Y., 2020, ApJ, 903, 150
Kansky J. et al., 2019, Astrophysics Source Code Library, record ascl:1905.004
Kriek M. et al., 2015, ApJS, 218, 15
Labbé I. et al., 2013, ApJ, 777, L19
Laporte N., Nakajima K., Ellis R. S., Zitrin A., Stark D. P., Mainali R., Roberts-Borsani G. W., 2017, ApJ, 851, 40
Le Fèvre O. et al., 2019, A&A, 625, A51
Livermore R. C., Finkelstein S. L., Lotz J. M., 2017, ApJ, 835, 113
Luridiana V., Morisset C., Shaw R. A., 2015, A&A, 573, A42
Mainali R. et al., 2018, MNRAS, 479, 1180
Mainali R. et al., 2020, MNRAS, 494, 719
Mainali R., Kollmeier J. A., Stark D. P., Simcoe R. A., Walth G., Newman A. B., Miller D. R., 2017, ApJ, 836, L14
Marques-Chaves R. et al., 2020, MNRAS, 499, L105
Maseda M. V. et al., 2013, ApJ, 778, L22
Maseda M. V. et al., 2014, ApJ, 791, 17
Maseda M. V. et al., 2017, A&A, 608, A4
McLean I. S. et al., 2012, in McLean I. S., Ramsay S. K., Takami H., eds, Proc. SPIE Conf. Ser. Vol. 8446, Ground-based and Airborne Instrumentation for Astronomy IV. SPIE, Bellingham, p. 84460J
McLure R. J. et al., 2013, MNRAS, 432, 2696
Momcheva I. G. et al., 2016, ApJS, 225, 27
Nakajima K. et al., 2018, A&A, 612, A94
Oemler A., Clardy K., Kelson D., Walth G., Villanueva E., 2017, Astrophysics Source Code Library, record ascl:1705.001
Oesch P. A., Bouwens R. J., Illingworth G. D., Labbé I., Stefanon M., 2018, ApJ, 855, 105
Oke J. B., Gunn J. E., 1983, ApJ, 266, 713
Pérez-Montero E., 2014, MNRAS, 441, 2663
Plat A., Charlot S., Bruzual G., Feltre A., Vidal-García A., Morisset C., Chevallard J., Todt H., 2019, MNRAS, 490, 978
Rasappu N., Smit R., Labbé I., Bouwens R. J., Stark D. P., Ellis R. S., Oesch P. A., 2016, MNRAS, 461, 3886

Ravindranath S., Monroe T., Jaskot A., Ferguson H. C., Tumlinson J., 2020, ApJ, 896, 170
Reddy N. A. et al., 2018, ApJ, 869, 92
Rigby J. R., Bayliss M. B., Gladders M. D., Sharon K., Wuyts E., Dahle H., Johnson T., Peña-Guerrero M., 2015, ApJ, 814, L6
Sanders R. L. et al., 2016, ApJ, 816, 23
Sanders R. L. et al., 2020, MNRAS, 491, 1427
Saxena A. et al., 2020, A&A, 636, A47
Schmidt K. B. et al., 2017, ApJ, 839, 17
Senchyna P. et al., 2017, MNRAS, 472, 2608
Senchyna P., Stark D. P., 2019, MNRAS, 484, 1270
Senchyna P., Stark D. P., Chevallard J., Charlot S., Jones T., Vidal-García A., 2019, MNRAS, 488, 3492
Shapley A. E., Steidel C. C., Pettini M., Adelberger K. L., 2003, ApJ, 588, 65
Shim H., Chary R.-R., Dickinson M., Lin L., Spinrad H., Stern D., Yan C.-H., 2011, ApJ, 738, 69
Shirazi M., Brinchmann J., 2012, MNRAS, 421, 1043
Skelton R. E. et al., 2014, ApJS, 214, 24
Smit R. et al., 2014, ApJ, 784, 58
Smit R. et al., 2015, ApJ, 801, 122
Smit R. et al., 2018, Nature, 553, 178
Stark D. P. et al., 2014, MNRAS, 445, 3200
Stark D. P. et al., 2015a, MNRAS, 450, 1846
Stark D. P. et al., 2015b, MNRAS, 454, 1393
Stark D. P. et al., 2017, MNRAS, 464, 469
Stark D. P., 2016, ARA&A, 54, 761
Stark D. P., Schenker M. A., Ellis R., Robertson B., McLure R., Dunlop J., 2013, ApJ, 763, 129
Steidel C. C., Strom A. L., Pettini M., Rudie G. C., Reddy N. A., Trainor R. F., 2016, ApJ, 826, 159
Strom A. L., Steidel C. C., Rudie G. C., Trainor R. F., Pettini M., 2018, ApJ, 868, 117
Tang M., Stark D. P., Chevallard J., Charlot S., 2019, MNRAS, 489, 2572 (T19)
Thuan T. X., Izotov Y. I., 2005, ApJS, 161, 240
Topping M. W., Shapley A. E., Reddy N. A., Sanders R. L., Coil A. L., Kriek M., Mobasher B., Siana B., 2020, MNRAS, 495, 4430
van der Wel A. et al., 2011, ApJ, 742, 111
Vanzella E. et al., 2008, A&A, 478, 83
Vanzella E. et al., 2016, ApJ, 821, L27
Vanzella E. et al., 2017, ApJ, 842, 47
Vanzella E. et al., 2020, MNRAS, 491, 1093
Vidal-García A., Charlot S., Bruzual G., Hubeny I., 2017, MNRAS, 470, 3532

This paper has been typeset from a TEX/LATEX file prepared by the author.